



## Efficient photocatalysts of TiO<sub>2</sub> nanocrystals-supported PtRu alloy nanoparticles for CO<sub>2</sub> reduction with H<sub>2</sub>O: Synergistic effect of Pt-Ru

Yuechang Wei<sup>a,\*</sup>, Xingxing Wu<sup>a</sup>, Yilong Zhao<sup>a</sup>, Lu Wang<sup>a</sup>, Zhen Zhao<sup>a,b,\*</sup>, Xiaotong Huang<sup>a</sup>, Jian Liu<sup>a</sup>, Jianmei Li<sup>a</sup>

<sup>a</sup> State Key Laboratory of Heavy Oil Processing, College of Science, China University of Petroleum, Beijing 102249, China

<sup>b</sup> Institute of Catalysis for Energy and Environment, Shenyang Normal University, Shenyang 110034, China



### ARTICLE INFO

#### Keywords:

TiO<sub>2</sub>nanocrystal  
Pt-Ru nanoparticles  
Synergic effect  
Photocatalytic CO<sub>2</sub>reduction  
Catalytic mechanism

### ABSTRACT

The photocatalytic reduction of CO<sub>2</sub> with H<sub>2</sub>O to chemical energy-rich molecules (CH<sub>4</sub> and CO) is significant to solve energy crisis. Herein, we have successfully fabricated the novel photocatalyst of bimetallic Pt-Ru alloy nanoparticles (NPs) selectively deposited on the {101} facet of TiO<sub>2</sub> nanocrystal via the photon-assisted gas bubbling-membrane reduction (P-GBMR) method. The photogenerated electrons and holes are enriched on the coexposed {101}-39% and {001}-61% facets of anatase TiO<sub>2</sub> nanocrystal, respectively. Noble metal (Pt, Ru and PtRu) NPs deposited on the TiO<sub>2</sub>-{101} facet can further improve the separation efficiency of photogenerated electron-hole pairs via the vectorial electron transfer of TiO<sub>2</sub>→PtRu. Pt/TiO<sub>2</sub> catalyst with enriched surface photogenerated electrons shows the relative high formation rate of CH<sub>4</sub> (22.9 μmol g<sup>-1</sup> h<sup>-1</sup>) and H<sub>2</sub> (52.8 μmol g<sup>-1</sup> h<sup>-1</sup>), while Ru/TiO<sub>2</sub> catalyst with strong adsorption/activation capability for CO<sub>2</sub> prefers to improve the selectivity to CO product (65.1%). The possible mechanism for CO<sub>2</sub> reduction is proposed and discussed: The formation of H-containing intermediate and the adsorption/activation property for CO<sub>2</sub> are two important determining steps for improving photocatalytic CO<sub>2</sub> reduction with H<sub>2</sub>O to CH<sub>4</sub> product. PtRu/TiO<sub>2</sub> catalyst with the synergic effect of Pt and Ru components exhibits the best catalytic performance for CO<sub>2</sub> reduction with H<sub>2</sub>O to CH<sub>4</sub> product under simulated solar irradiation, i.e., its formation rate of CH<sub>4</sub> (38.7 μmol g<sup>-1</sup> h<sup>-1</sup>) is about 29-fold of commercial P25, its selectivity to CH<sub>4</sub> product is 93.7% and its apparent quantum efficiency for CO<sub>2</sub> conversion is 0.98%. It expected to be a new heuristic on the development of high efficient photocatalysts for application to light-chemical energy conversion.

### 1. Introduction

The rapid growth of CO<sub>2</sub> concentration in atmosphere resulting from the consumption of fossil fuels has caused the global climate change, which is regarded as one of the greatest environmental crises in this century [1,2]. The mimicking photosynthesis of green plants (artificial photosynthesis), using the energy in sunlight to knit together hydrocarbon fuels (CH<sub>4</sub>, CO and so on) from water and CO<sub>2</sub>, has attracted considerable attention in recent years [3–5]. Since the pioneering reported by Fujishima and co-authors on the photoelectrocatalytic reduction of CO<sub>2</sub> to hydrocarbon compounds [6], a variety of high-performance photocatalysts for CO<sub>2</sub> conversion with H<sub>2</sub>O to fuels have been reported, such as metal oxides, metal sulfides and oxynitride semiconductor [7–11]. However, the practical applications for photocatalytic CO<sub>2</sub> conversion are still limited by the low formation rate of reduced products and the low efficiency of light-chemical energy

conversion because of the rapid recombination of photogenerated electrons and holes. Therefore, the well-developed characteristics of high-performance photocatalysts with the suitable band gap often present the high separation efficiency of photogenerated electrons and holes [12–14].

In the past several decades, TiO<sub>2</sub> is one of the most widely investigated semiconductor materials because of its nontoxicity, cost inexpensive, corrosion resistant and long-term stability [15–21]. Among the phase structures of anatase, rutile and brookite, anatase TiO<sub>2</sub>-based catalysts with more negative of conduction band usually show the high photocatalytic activity for CO<sub>2</sub> conversion. The photocatalytic activity of anatase TiO<sub>2</sub> nanocrystal is related to the exposed percentage of {001}, {010} and {101} low-index facets whose average surface energies are 0.90, 0.53 and 0.44 J m<sup>-2</sup> in single anatase nanocrystals, respectively [22]. The {001} facet with high surface energy is beneficial for enhancing the adsorption property for H<sub>2</sub>O and CO<sub>2</sub> reactants. After

\* Corresponding authors at: 18# Fuxue Road, Chang Ping District, Beijing, 102249, China.

E-mail addresses: [weiyic@cup.edu.cn](mailto:weiyic@cup.edu.cn) (Y. Wei), [zhenzhao@cup.edu.cn](mailto:zhenzhao@cup.edu.cn) (Z. Zhao).

the absorption of photons,  $\text{TiO}_2$  nanocrystal with coexposed  $\{101\}$  and  $\{001\}$  facets is excited to produce the photogenerated electron-hole pairs. The  $\{101\}$  facet can selectively gather the surface photogenerated electrons, while surface photogenerated holes remain on the surface of  $\{001\}$  facet, because of their different electronic energy levels and the distribution of potential trapping sites [23]. Thus, the coexposed  $\{101\}$  and  $\{001\}$  facets in one anatase  $\text{TiO}_2$  nanocrystal can form the surface heterojunction, which is favorable for the separation of photogenerated charges. The optimal percentage of  $\{101\}$  and  $\{001\}$  facets in an anatase  $\text{TiO}_2$  nanocrystal can further improve separation efficiency of photogenerated charges and enhance photocatalytic activity for  $\text{CO}_2$  reduction with  $\text{H}_2\text{O}$  [24,25]. However, the photocatalytic performances of pure anatase  $\text{TiO}_2$  nanocrystal with coexposed  $\{101\}$  and  $\{001\}$  facets for  $\text{CO}_2$  reduction still need to be improved to meet the industrialized application, which can be realized by enhancing the separation efficiency of photogenerated electron-hole pairs and increasing the sufficient surface adsorption sites for  $\text{CO}_2$  [26–29].

For the reaction nature of photocatalytic  $\text{CO}_2$  reduction with  $\text{H}_2\text{O}$ , the formation of  $\text{CH}_4$  molecule is one process of eight electrons, eight hydrogen protons and one  $\text{CO}_2$  molecule. Thus, the surface enrichments of photogenerated electrons and adsorbed reactant molecules are very critical to improve formation rate and selectivity of  $\text{CH}_4$  product [30]. It is well known that supported noble metal nanoparticles (NPs) can suppress the recombination of photogenerated electron-hole pairs and improve the utilization efficiency of photogenerated electrons [31–34]. For example, photogenerated electrons of  $\text{TiO}_2$  nanocrystals can be rapidly transferred and trapped by supported Pt NPs as a reservoir of photoelectrons because of its lower Fermi levels in comparison with the conduction band edge of  $\text{TiO}_2$ , and the Schottky barrier formed at the interface of heterojunction can suppress the electronic backflow [35–37]. Supported Pt NPs with enriched photoelectrons are beneficial for the improving photocatalytic activity, especially to the formation of  $\text{H}_2$  product from water splitting via bi-electron reduction process [38,39]. In order to further enhance photocatalytic activity of  $\text{CO}_2$  conversion, the enhancing adsorption and activation property for  $\text{CO}_2$  reactant is a potential solution [40,41]. It is well known that supported Ru catalysts are widely used in the photocatalytic  $\text{CO}_2$  reduction to CO product due to the strong  $\text{CO}_2$  activation property of supported Ru NPs [42,43]. Thus, supported bimetallic NPs with Pt and Ru components are potential to further improve the separation efficiency of photogenerated electron-hole pairs and enhance the adsorption/activation capacity for reactants in artificial photosynthesis reaction. Based on the above preeminent features, the fabrication of fine structured photocatalyst with PtRu NPs deposited on the  $\{101\}$  facet of  $\text{TiO}_2$  nanocrystal, which combines of both the surface heterojunction between coexposed  $\{101\}$  and  $\{001\}$  facets and the synergic effect of Pt and Ru components, is expected to bring high catalytic activity for photocatalytic  $\text{CO}_2$  reduction.

Herein, the novel photocatalysts of monometallic Pt, Ru and bimetallic Pt-Ru nanoparticles (NPs) selectively deposited on the  $\{101\}$  facet of single  $\text{TiO}_2$  nanocrystal with coexposed facets of  $\{001\}$ -61% and  $\{101\}$ -39% were successfully fabricated by the photon-assisted gas bubbling-membrane reduction (P-GBMR) method. The photogenerated electrons enriched on the surface of  $\{101\}$  facet result in the selective deposition of noble metal NPs on the surface of  $\text{TiO}_2$  nanocrystal, which can further improve the efficient separation of photogenerated electron-

hole pairs. Pt/ $\text{TiO}_2$  and Ru/ $\text{TiO}_2$  photocatalysts showed high selectivity to  $\text{CH}_4$  and CO products from  $\text{CO}_2$  conversion, respectively. PtRu/ $\text{TiO}_2$  photocatalyst with bimetallic synergic effect of Pt and Ru components exhibits the best catalytic performance for  $\text{CO}_2$  conversion with  $\text{H}_2\text{O}$  far exceeding the unitary supported noble metal system. The mechanism of PtRu/ $\text{TiO}_2$  photocatalyst for  $\text{CO}_2$  reduction with  $\text{H}_2\text{O}$  was discussed and elaborated. PtRu/ $\text{TiO}_2$  catalyst is an excellent system not only for fundamental surface chemical research, but also for light-chemical energy conversion.

## 2. Experimental section

### 2.1. Sample preparation

#### 2.1.1. Synthesis of anatase $\text{TiO}_2$ nanocrystals

The synthesis of truncated octahedral bipyramid anatase  $\text{TiO}_2$  nanocrystal was carried out through a simple hydrothermal method. In a typical experiment, tetrabutyl titanate [ $\text{Ti}(\text{OBu})_4$ , 98%, Aldrich] (32.0 mL) and aqueous hydrofluoric acid solution [HF, 40%, Sinopharm Chemical Reagent Co., Ltd.] (4 mL) were added into a dried Teflon-lined stainless steel autoclave with a capacity of 100 mL, the mixture was allowed to react for 24 h at 180 °C in an electric oven, and then cool to room temperature. The solid precipitation was washed and collected by centrifugation using absolute ethanol and deionized water for three times in order to remove thoroughly the residual contamination. After vacuum drying at 80 °C for 12 h, anatase  $\text{TiO}_2$  nanocrystals with coexposed facets of  $\{001\}$  and  $\{101\}$  were finally obtained.

#### 2.1.2. Synthesis of PtRu/ $\text{TiO}_2$ photocatalysts

The novel photocatalysts of monometallic Pt, Ru and bimetallic Pt-Ru alloy NPs selectively deposited on the  $\{101\}$  facet of single anatase  $\text{TiO}_2$  nanocrystal were designed and synthesized by the photon-assisted gas bubbling-membrane reduction (P-GBMR) method. The schematic representation of the preparation processing for PtRu/ $\text{TiO}_2$  photocatalyst is shown in Fig. 1. The typical two-step procedures were described as follows: Firstly, the anatase  $\text{TiO}_2$  nanocrystal with coexposed facets of  $\{001\}$  and  $\{101\}$  is mixed with noble metal precursor ( $\text{PtCl}_4$ ,  $\text{RuCl}_3$ ) solution. And then the mixtures were radiated by UV-vis light with the wavelength of 200–800 nm for 30 min. The photogenerated electrons enriched on the surface of  $\{101\}$  facet could react with noble metal precursors, so the process can control the nucleation process of noble metal seeds selectively deposited on the  $\{101\}$  facet of anatase  $\text{TiO}_2$  nanocrystal. Secondly, the  $\text{NaBH}_4$  solution as the reducing agent was introduced into the mixture solution via the gas bubbling-membrane reduction (GBMR) device in order to accelerate the growth process of supported noble metal NPs [44,45]. The GBMR process can control the growth process of noble metal (Pt, Ru and PtRu) seeds on the surface of anatase  $\text{TiO}_2$ - $\{101\}$  facet via highly homogeneous dispersion of reducing agent ( $\text{NaBH}_4$ ) using the ceramic membrane tubes. After supported PtRu NPs, the color of samples changed from white to light gray. The procedure of supported monometallic Pt and Ru NPs is same as that of supported PtRu NPs. The loading amounts of supported Pt, Ru and PtRu NPs in the photocatalysts are 4.0 wt% in theory. Finally, after the processes of centrifugation, washing, drying and calcination in an oven at 300 °C for 2 h, the desired Pt/ $\text{TiO}_2$ , Ru/ $\text{TiO}_2$  and PtRu/ $\text{TiO}_2$  photocatalysts were obtained.

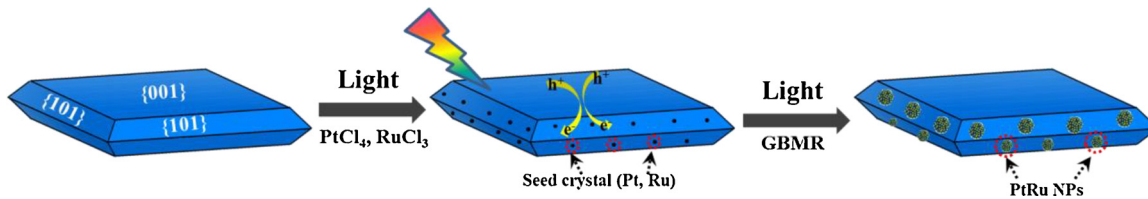


**Fig. 1.** The schematic for synthesis of typical PtRu NPs selectively deposited on the  $\{101\}$  facet of  $\text{TiO}_2$  nanocrystal via the photon-assisted GBMR (P-GBMR) method.

## 2.2. Characterization

The morphology and nanostructure features were investigated on a transmission electron microscope (TEM, JEOL JEM 2100) equipped with a field emission source at an accelerating voltage of 200 kV. The exposed percentage of {001} facets can be calculated based on the sizes of the thickness, the side length and the intersection angle of one truncated octahedral bipyramidal anatase  $\text{TiO}_2$  nanocrystal. High angle annular dark field-scanning transmission electron microscope (HAADF-STEM) images and energy-dispersive X-ray (EDX) spectroscopy analysis were carried out on an FEI Tecnai G2 F20 TEM operating at 200 kV. The  $\text{N}_2$  adsorption/desorption isotherm at  $-196^\circ\text{C}$  was obtained on an automated gas sorption analyzer (Quantachrome Autosorb-iQ, USA). The specific surface area was calculated by the Brunauer-Emmett-Teller (BET) method. The actual amounts of Pt and Ru in the catalysts were determined by inductive coupled plasma optical emission spectrometry (ICP-OES, Perkin Elmer, OPTIMA 7300 V). The crystal phase informations of all as-prepared samples were analyzed with a powder X-ray diffractometer (Shimadzu XRD 6000). The microscopic phase structure was further obtained on a Renishaw Micro-Raman System 2000 spectrometer using the laser line of 532 nm. The surface states of Pt and Ru elements on the surface of  $\text{TiO}_2$  nanocrystals were investigated by X-ray photoelectron spectra (XPS) using a Perkin-Elmer PHI-1600 ESCA spectrometer with Mg Ka emission. Photoluminescence (PL) emission spectroscopy was carried out on an Edinburgh Instruments Xe900 equipped with a Xe lamp, and the excitation wavelength was set at 380 nm. Transient photocurrent responses were carried out on an electrochemical workstation (CHI660E) in the saturated solution of  $\text{Na}_2\text{SO}_4$  with a three-electrode configuration, which all as-prepared catalysts, the saturated Ag/AgCl, a platinum foil were used to as the working photoelectrode, the reference and the counter electrode, respectively. The catalysts were illuminated under a 300 W Xe lamp. Temperature-programmed desorption of  $\text{CO}_2$  ( $\text{CO}_2$ -TPD) experiments were carried out on an online gas chromatograph (GC) equipped with a thermal conductivity detector (TCD). The catalyst (100 mg) was pretreated in Ar gas ( $60 \text{ cm}^3 \text{ min}^{-1}$ ) at  $150^\circ\text{C}$  for 1 h and then cooled down to room temperature. Next, the catalyst was exposed to  $\text{CO}_2$  gas with flow rate of  $30 \text{ cm}^3 \text{ min}^{-1}$  for 30 min in order to ensure the sufficient adsorption of  $\text{CO}_2$ . Before desorption, the sample was purged by Ar gas for 1 h. Subsequently,  $\text{CO}_2$  desorption was carried out by using an Ar flow ( $30 \text{ cm}^3 \text{ min}^{-1}$ ) in the range of  $30\text{--}400^\circ\text{C}$  at a heating rate of  $10^\circ\text{C min}^{-1}$ . Hydrogen temperature-programmed desorption ( $\text{H}_2$ -TPD) experiments were carried out on same apparatus of  $\text{CO}_2$ -TPD. The catalyst (0.1 g) was pretreated in Ar gas ( $60 \text{ cm}^3 \text{ min}^{-1}$ ) at  $350^\circ\text{C}$  for 1 h. After cooling down to room temperature under Ar flow, high-purity  $\text{H}_2$  flow ( $50 \text{ ml min}^{-1}$ ) was introduced to saturate the catalyst surface with hydrogen for 30 min. And then the sample was purged by Ar flow ( $30 \text{ cm}^3 \text{ min}^{-1}$ ) for 30 min. Finally,  $\text{H}_2$ -TPD measurements were carried out in the range of  $30\text{--}400^\circ\text{C}$  ( $10^\circ\text{C min}^{-1}$ ) under Ar flow ( $30 \text{ cm}^3 \text{ min}^{-1}$ ). The signal of  $\text{H}_2$  desorption was monitored by GC-TCD.

## 2.3. Photocatalytic reduction of $\text{CO}_2$ with $\text{H}_2\text{O}$

Photocatalytic performances of  $\text{CO}_2$  reduction with  $\text{H}_2\text{O}$  over the catalysts were carried out in a gas-closed circulation system (Perfect Light Company, Beijing, China), and a 300 W Xe lamp with wavelength of 320–780 nm was used as the light source. The catalysts (100 mg) were well-distributed onto a watch-glass reactor with the basal diameter of 6.5 cm. Before the light irradiation, the photo reactor system was thoroughly vacuum-treated, and then  $\text{CO}_2$  gas and distilled water with saturated vapor pressure at  $30^\circ\text{C}$  were introduced into the circulation system. The deionized water (2 mL) was also injected into the bottom of the reactor. The intensity of incident light was  $80 \text{ mW cm}^{-2}$  determined by a spectroradiometer (FZ-A, Photoelectric Instrument Factory of Beijing Normal University). The photocatalytic reduction of  $\text{CO}_2$  was carried out over a period of 8 h. During the light irradiation,

the  $\text{H}_2$ , CO, and  $\text{CH}_4$  products in the reactor were analyzed by an online gas chromatograph (GC-9560, HuaAiSePu Corp., Shanghai, China) with a flame ionization detector (FID) and a thermal conductivity detector (TCD) each interval of 60 min. The quantification of gas products was based on the external standard method with the use of a calibration curve. Commercial P25 (Degussa Co.) was selected as the reference catalyst for photocatalytic  $\text{CO}_2$  reduction. The photocatalytic performances for  $\text{CO}_2$  reduction with  $\text{H}_2\text{O}$  were evaluated by the formation rates and the selectivities of  $\text{H}_2$ , CO and  $\text{CH}_4$  products. And the selectivities for  $\text{CO}_2$  reduction ( $S_{\text{CO}_2}$ ) were evaluated on an electron basis of  $\text{H}_2$ , CO, and  $\text{CH}_4$  products, as following the equation:

$$S_{\text{CO}_2} [\%] = \frac{\text{Number of } \text{CH}_4 \times 8 + \text{Number of } \text{CO} \times 2}{\text{Number of } \text{H}_2 \times 2 + \text{Number of } \text{CH}_4 \times 8 + \text{Number of } \text{CO} \times 2} \times 100\%$$

The selectivities for  $\text{CO}_2$  conversion to  $\text{CH}_4$  ( $S_{\text{CH}_4}$ ) and CO ( $S_{\text{CO}}$ ) products were obtained by the ratios of [CO] or [ $\text{CH}_4$ ] amounts to sum ([CO] + [ $\text{CH}_4$ ]) amounts. The apparent quantum efficiency (AQE) values of all the catalysts were obtained under the same photocatalytic reaction condition, and the irradiation light with wavelength of 380 nm obtained by using a band-pass filter (full width at half maximum 15 nm) was used as the light source. The incident flux was determined by a spectroradiometer. The AQE values for  $\text{CH}_4$  and CO products were calculated according to the following equation:

$$\text{AQE} [\%] = \frac{\text{Number of } \text{CH}_4 \times 8 + \text{Number of } \text{CO} \times 2}{\text{Number of Incident Photos}} \times 100\%$$

## 3. Results and discussion

### 3.1. The results of TEM and STEM images

The nanostructures of  $\text{TiO}_2$  nanocrystal,  $\text{Pt/TiO}_2$ ,  $\text{Ru/TiO}_2$  and  $\text{PtRu/TiO}_2$  catalysts were investigated by TEM and HRTEM images, and the results are shown in Fig. 2. For  $\text{TiO}_2$  nanocrystals, the hexagons and square as top and side projections of truncated octahedral bipyramidal are observed obviously. The lateral isosceles trapezoid of truncated octahedral bipyramidal nanocrystals corresponds to {101} facet, and the top and bottom facets are the {001} facet [46]. As shown in inset of Fig. 2a, the interfacial angle between {101} and {001} facets is  $68.3^\circ$ . The thickness and the length of top and middle sides are 9.5, 34 and 39 nm, respectively. Thus, the exposed percentage of  $\text{TiO}_2$ -{001} facet can be calculated by the equation listed in Fig. S1, and the values of coexposed {001} and {101} facets are 61% and 39%, respectively [47]. The high exposed percentage of {001} facet with big surface energy is beneficial for enhancing the adsorption property for  $\text{H}_2\text{O}$  and  $\text{CO}_2$  reactants, and the coexposed {101} and {001} facets on a single anatase  $\text{TiO}_2$  nanocrystal can form a surface heterojunction owing to their different band edge positions, which is favorable to the separation of photogenerated electron-hole pairs. The homogeneously truncated octahedral bipyramidal structure of  $\text{TiO}_2$  nanocrystals with the average particle size of 35 nm is also observed by SEM image in Fig. S2. As shown in inset of Fig. 2a, the lattice spacing is ca. 0.24 nm, which is corresponding to the {004} facets of anatase  $\text{TiO}_2$  nanocrystal. After introduction of supported Pt NPs, it is clearly observed that a mass of bare Pt NPs are selectively deposited on the {001} facet of  $\text{TiO}_2$  nanocrystals in Fig. 2b, which is attributed to the selective nucleation process of noble metal seeds on the {101} facet of anatase  $\text{TiO}_2$  nanocrystals due to the photogenerated electrons enriched on the surface of {101} facet. Fig. S3 shows the size distribution of supported Pt NPs is in the narrow range of 2–6 nm, and the average diameter is about 4.2 nm via statistical analyses of more than 100 Pt NPs. As shown in inset of Fig. 2b, the lattice fringes (0.23 nm) of one hemispherical Pt NP exhibit clearly the exposed (111) facet, and the crystal fusion domain at the

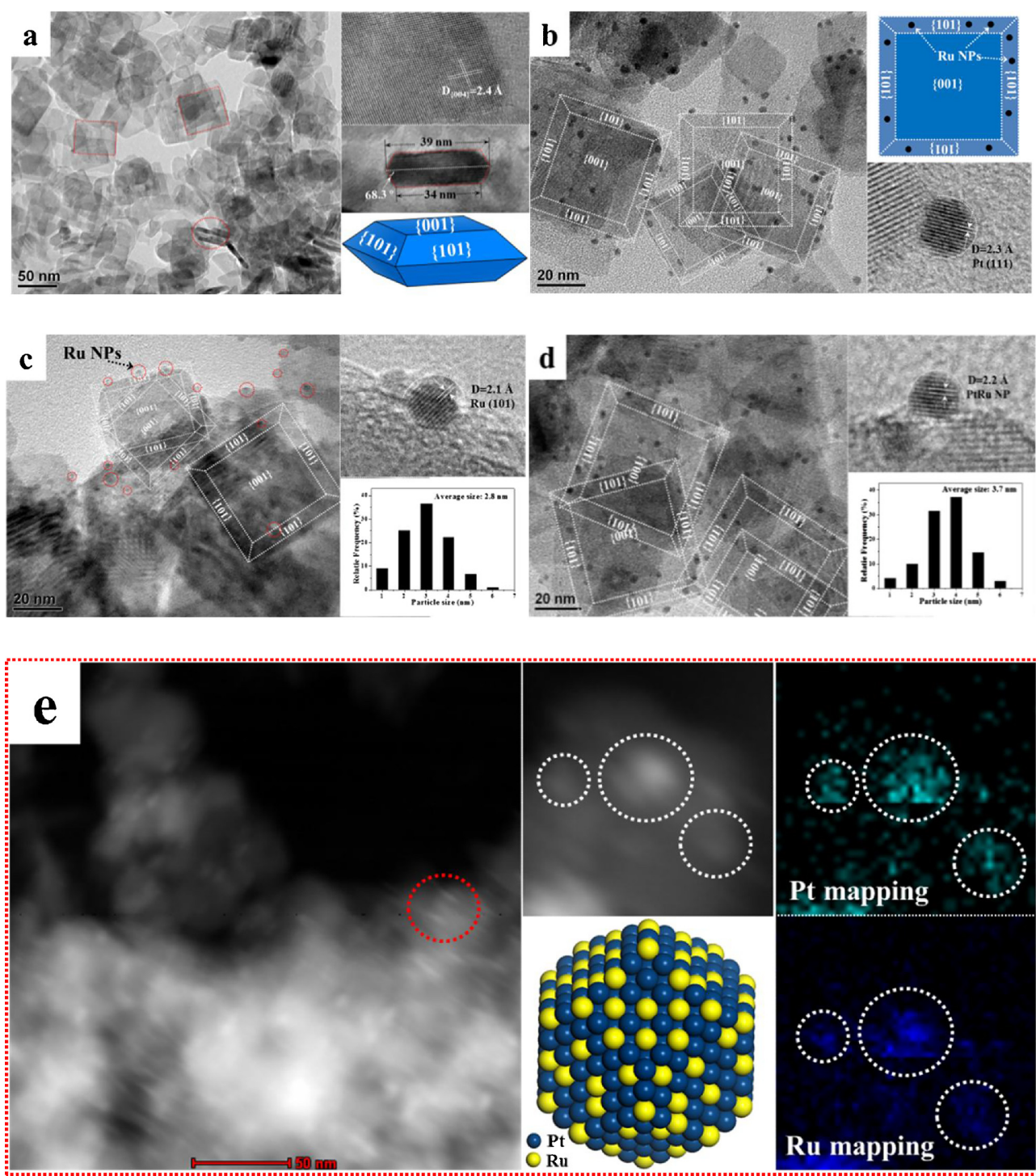


**Fig. 2.** TEM, HRTEM images and size distributions of supported Pt, Ru and PtRu NPs over TiO<sub>2</sub> nanocrystal (a), Pt/TiO<sub>2</sub> (b), Ru/TiO<sub>2</sub> (c) and PtRu/TiO<sub>2</sub> (d) catalysts. (e) HAADF-STEM and EDS elemental mapping images of PtRu/TiO<sub>2</sub> catalyst.

phase interface of Pt-TiO<sub>2</sub> shows a strong lattice distortion. It indicates that there is a tight contact interface between Pt NPs and TiO<sub>2</sub> nanocrystals, which is beneficial to the subsequent efficient electron transfer after light irradiation. For Ru/TiO<sub>2</sub> catalyst in Fig. 2c, the Ru NPs are also almost selectively deposited on the {001} facet of TiO<sub>2</sub> nanocrystals. Fig. S4 shows one TEM image of fabricated intermediate with Ru seeds (sizes < 1.0 nm) selective deposited on the {101} faces of TiO<sub>2</sub> after UV-vis light (200–800 nm) irradiation for 30 min, which is direct proof for selective deposition mechanism of P-GBMR method. As shown in inset of Fig. 2c, the size distribution of supported Ru NPs on the {101}

facet surface of TiO<sub>2</sub> nanocrystal is in the narrow range of 1–6 nm, and the average diameter (2.8 nm) is smaller obviously than that of supported Pt NPs. And the lattice fringes of one hemispherical Ru NP is 0.21 nm, which is assigned to the exposed (101) facet of supported Ru NPs, and the crystal fusion domain at the phase interface of Ru-TiO<sub>2</sub> indicates the strong metal-support interaction.

As shown in Fig. 2d, a mass of bimetallic PtRu NPs are selectively deposited on the {101} facet of anatase TiO<sub>2</sub> nanocrystal. The truncated octahedron bipyramidal nanostructure of anatase TiO<sub>2</sub> nanocrystal has not changed, indicating that supported PtRu NPs have not influenced to

the nanostructure of  $\text{TiO}_2$  nanocrystal during the synthesis process of P-GBMR method. The size distribution of supported PtRu NPs is in the narrow range of 1–6 nm in inset of Fig. 2d, and the average diameter (3.7 nm) is between supported Ru and Pt NPs. The lattice fringe of one hemispherical Pt-Ru alloy NP is 0.22 nm. In order to further observe the morphology and composition of PtRu/ $\text{TiO}_2$  catalyst, the HAADF-STEM and EDS elemental mapping images were carried out, and the results are shown in Fig. 2e. Supported PtRu NPs are homogeneously dispersed on the surface of anatase  $\text{TiO}_2$  nanocrystal, which is in agreement with the result of TEM images. The composition of supported PtRu NPs is further observed by means of HAADF-STEM-EDS elemental mappings in inset of Fig. 2e. The elemental dispersion of supported Pt NPs (light blue) is similar to that of supported Ru NPs (dark blue), indicating that it is an alloy structure. It suggests that the mixed Ru and Pt precursors were reduced simultaneously. In other words, it is realized to the formation of supported bimetallic Pt-Ru alloy NPs. Therefore, a ternary PtRu- $\text{TiO}_2$  nanojunction system with a tight electronic contact and synergistic effect of Pt-Ru ensures the efficient transfer efficiency of photogenerated electron and the subsequent photocatalysis.

### 3.2. The results of XRD characterization

The phase structures of  $\text{TiO}_2$  nanocrystal, Pt/ $\text{TiO}_2$ , Ru/ $\text{TiO}_2$  and PtRu/ $\text{TiO}_2$  catalysts were investigated by XRD patterns, and the result is shown in Fig. 3. It is noted that there are seven diffraction peaks (2θ) of  $\text{TiO}_2$  nanocrystal centered at 25.3, 37.8, 48.0, 53.9, 55.1, 62.7 and 75.0°, which are indexed to the (101), (004), (200), (105), (211), (204) and (215) lattice planes of the tetragonal anatase phase structure of  $\text{TiO}_2$  (PDF# 21-1272), respectively. There is not any diffraction peak assigned to other phase of  $\text{TiO}_2$ , indicating that the phase structure of anatase  $\text{TiO}_2$  nanocrystal is single and pure. It is well known that the photogenerated electrons and holes are enriched on the surface of {101} and {001} facets, respectively. [48] And the surface heterojunction between coexposed {101} and {001} facets on a perfect single crystal of anatase  $\text{TiO}_2$  is helpful for enhancing separation of photogenerated electron-hole pairs. After introduction of supported Pt, Ru and PtRu alloy NPs, the diffraction peaks belonging to  $\text{TiO}_2$  have not changed, and the characteristic diffraction peaks corresponding to Pt, Ru and PtRu alloy NPs were not detected. It suggests that the sizes of supported Pt, Ru and PtRu alloy NPs are smaller than the detection limit of XRD spectra. The average crystalline sizes of anatase  $\text{TiO}_2$  nanocrystals are determined by Scherer equation using the intensity of the most prominent (101) peak, and the results are shown in Table 1. Their average crystalline sizes are  $36 \pm 1$  nm, which is accordance with the TEM and SEM images. In addition, Table 1 shows the structural parameters of  $\text{TiO}_2$  nanocrystal, Pt/ $\text{TiO}_2$ , Ru/ $\text{TiO}_2$  and PtRu/ $\text{TiO}_2$  catalysts. After introduction of supported Pt, Ru and PtRu NPs, the structural parameters of the catalysts have not changed obviously. For example,

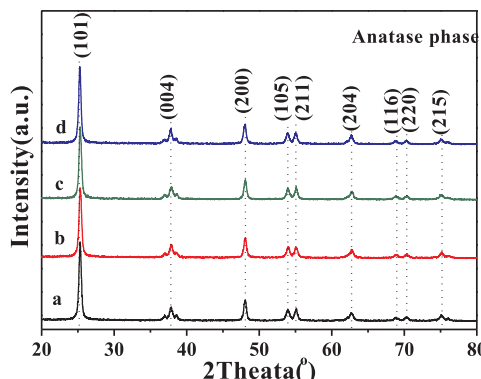


**Fig. 3.** XRD patterns of  $\text{TiO}_2$  nanocrystal (a), Pt/ $\text{TiO}_2$  (b), Ru/ $\text{TiO}_2$ (c) and PtRu/ $\text{TiO}_2$  (d) photocatalysts.

**Table 1**

The surface areas, the pore volumes, the crystal parameters, the average sizes and the actual contents of Pt-Ru NPs of  $\text{TiO}_2$  nanocrystal, Pt/ $\text{TiO}_2$ , Ru/ $\text{TiO}_2$  and PtRu/ $\text{TiO}_2$  catalysts.

Catalyst	Size of Pt-Ru NP (nm) <sup>a</sup>	$S_{\text{BET}}$ ( $\text{m}^2 \text{g}^{-1}$ ) <sup>b</sup>	$V_p$ ( $\text{cm}^3 \text{g}^{-1}$ ) <sup>c</sup>	Size of $\text{TiO}_2$ (nm) <sup>d</sup>	Pt content (wt%) <sup>e</sup>	Ru content (wt%) <sup>e</sup>
TiO <sub>2</sub>	—	32.1	0.23	37	—	—
Pt/TiO <sub>2</sub>	4.2	30.8	0.21	35	3.6	—
Ru/TiO <sub>2</sub>	2.8	33.0	0.24	37	—	3.7
PtRu/TiO <sub>2</sub>	3.7	31.6	0.22	36	1.8	1.9

<sup>a</sup> The average sizes of Pt-Ru NP determined by TEM images.

<sup>b</sup> Surface area obtained by BET method.

<sup>c</sup> Pore volume determined by BET method.

<sup>d</sup> Determined by XRD using Scherrer equation with the intensity of (101) peak.

<sup>e</sup> Determined by ICP-OES.

the surface areas and pore volumes of all catalysts determined by BET method are  $31.1 \pm 1 \text{ m}^2 \text{ g}^{-1}$  and  $0.22 \pm 0.2 \text{ cm}^3 \text{ g}^{-1}$ , respectively. And the actual contents of Pt and Ru in the catalysts determined by ICP-OES are close to the theoretical values (4 wt %).

### 3.3. The results of Raman characterization

The strong scattering properties of Raman spectra can further obtain and analyse the phase structure characters of the catalysts. Fig. 4 exhibits the Raman spectra of  $\text{TiO}_2$  nanocrystal, Pt/ $\text{TiO}_2$ , Ru/ $\text{TiO}_2$  and PtRu/ $\text{TiO}_2$  catalysts. The four characterized Raman bands centered at 144, 397, 517, and 638  $\text{cm}^{-1}$  over all the catalysts are observed clearly, which are assigned to the Raman-active  $E_g(1)$ ,  $B_{1g}(1)$ ,  $A_{1g} + B_{1g}(2)$ , and  $E_g(2)$  modes of tetragonal anatase phase structure of  $\text{TiO}_2$ , respectively [49]. The  $E_g$  peaks appeared at 144 and 638  $\text{cm}^{-1}$  are assigned to the symmetrical stretching vibration of O-Ti-O bond on the {101} facet surface of  $\text{TiO}_2$ , while the  $A_{1g}$  and  $B_{1g}$  peaks are related to the bending vibration of O-Ti-O bond on the {001} facet surface of  $\text{TiO}_2$ . Based the intensity of  $E_g$  and  $A_{1g}$  peaks, the exposed percentage of  $\text{TiO}_2$ -{001} facet (62%) can be obtained [50], which is accordance with the results obtained by TEM image. The single anatase phase structure of  $\text{TiO}_2$  support is further confirmed, which is consistent with the result of XRD. After introduction of supported Pt, Ru and PtRu alloy NPs, the intensity and position of characterized Raman bands have not changed obviously. It further indicates that supported Pt, Ru and PtRu NPs have not influenced to the phase structure and morphology of  $\text{TiO}_2$  nanocrystal.

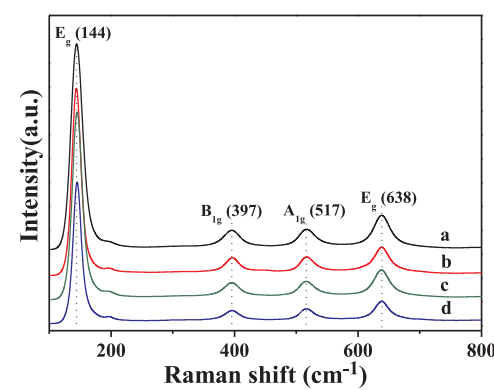


**Fig. 4.** Raman spectra of  $\text{TiO}_2$  nanocrystal (a), Pt/ $\text{TiO}_2$  (b), Ru/ $\text{TiO}_2$ (c) and PtRu/ $\text{TiO}_2$  (d) photocatalysts.

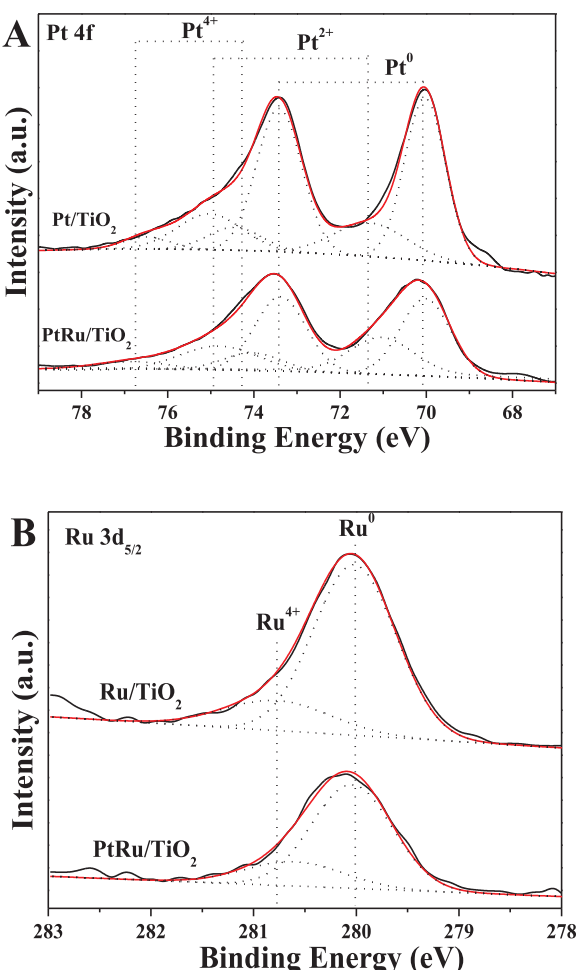


**Fig. 5.** XPS of Pt 4f (A) and Ru 3d (B) of Pt/TiO<sub>2</sub>, Ru/TiO<sub>2</sub> and PtRu/TiO<sub>2</sub> catalysts. The XPS of Ru 3d<sub>3/2</sub> overlaps with C 1 s, so XPS of Ru 3d<sub>5/2</sub> is only exhibited in figure (B).

#### 3.4. The results of XPS characterization

In order to obtain the effect of bimetallic Pt-Ru alloy NPs on the electronic properties of the surface elements (Pt and Ru), XPS spectra of Pt 4f and Ru 3d regions for Pt/TiO<sub>2</sub>, Ru/TiO<sub>2</sub> and PtRu/TiO<sub>2</sub> catalysts were performed, and the results are shown in Fig. 5 and Table 2. As shown in Fig. 5A, the Pt 4f XPS peak intensity of PtRu/TiO<sub>2</sub> catalyst is lower than that of Pt/TiO<sub>2</sub> catalyst due to the decreasing loading amount of Pt. The deconvolutions of Pt 4f XPS spectra were made by the standard procedure. The binding energy pairs corresponding to the spin-orbit coupling of Pt 4f<sub>7/2</sub> and Pt 4f<sub>5/2</sub> are located at 70.1 and 73.5 eV, 71.3 and 74.9 eV, 74.2 and 76.8 eV, which are assigned to Pt<sup>0</sup>, Pt<sup>2+</sup> and Pt<sup>4+</sup> species, respectively. It suggests that the metallic (Pt<sup>0</sup>) and ionic (Pt<sup>&+</sup>) species coexist in Pt/TiO<sub>2</sub> and PtRu/TiO<sub>2</sub> catalysts. The formation of ionic Pt<sup>&+</sup> (Pt<sup>2+</sup> and Pt<sup>4+</sup>) species are derived from

**Table 2**  
Surface compositions and oxidation states of Pt and Ru species derived from XPS analyses.

Samples	Pt species (%)				Ru species (%)	
	Pt <sup>0</sup>	Pt <sup>2+</sup>	Pt <sup>4+</sup>	Pt <sup>&amp;+<sup>a</sup></sup>	Ru <sup>0</sup>	Ru <sup>4+</sup>
Pt/TiO <sub>2</sub>	72.1	20.6	7.3	27.9	—	—
Ru/TiO <sub>2</sub>	—	—	—	—	78.6	21.4
PtRu/TiO <sub>2</sub>	59.5	31.3	9.2	40.5	72.5	27.5

<sup>a</sup> The Pt<sup>&+</sup> values are equal to the sum of Pt<sup>2+</sup> and Pt<sup>4+</sup>.

the electron transfer from Pt<sup>0</sup> to TiO<sub>2</sub> due to the strong metal-support interaction between metal (Pt)-support (TiO<sub>2</sub>), which is favorable to the vectorial electron transfer from excitation of TiO<sub>2</sub> to Pt driven by the low level of Pt-Fermi energy [51]. The relative proportions of Pt<sup>0</sup>, Pt<sup>2+</sup> and Pt<sup>4+</sup> species on the surface of catalysts were estimated by the fitting peak areas, and the results are showed in Table 2. The surface Pt<sup>&+</sup> concentration of PtRu/TiO<sub>2</sub> catalyst is 40.5%, which is significantly higher than that of Pt/TiO<sub>2</sub> catalyst (27.9%). It indicates that the synergic effect between Pt and Ru in Pt-Ru alloy NPs can increase the surface Pt<sup>&+</sup> concentration due to the decreasing d-electron density of Pt atoms, which is beneficial to sequent the photogenerated electron transfer from conduction band of TiO<sub>2</sub> to Pt.

The Ru 3d<sub>5/2</sub> XPS spectra of Pt/TiO<sub>2</sub> and PtRu/TiO<sub>2</sub> catalysts are shown in Fig. 5B. The XPS spectra of Ru 3d<sub>3/2</sub> are not presented due to the interference of C 1 s XPS spectrum located at 284 eV. The binding energies of the spin-orbit coupling Ru 3d<sub>5/2</sub> are located at 280.0 and 280.9 eV, which are assigned to Ru<sup>0</sup> and Ru<sup>4+</sup> species, respectively. It suggests that both metallic (Ru<sup>0</sup>) and ionic (Ru<sup>4+</sup>) species coexist on the surface of anatase TiO<sub>2</sub> nanocrystal. As shown in Table 2, the surface percent of Ru<sup>4+</sup> species over Ru/TiO<sub>2</sub> catalyst is 21.4%, while the value increases to 27.5% for PtRu/TiO<sub>2</sub> catalyst. It also indicates that the synergic effect between Pt and Ru in Pt-Ru alloy NPs can increase the surface Ru<sup>&+</sup> concentration. It is generally accepted that Pt<sup>&+</sup> and Ru<sup>&+</sup> species acting as electron trapping sites of photoexcited TiO<sub>2</sub> can improve the vectorial electron transfer from TiO<sub>2</sub> to PtRu NPs, which can decrease the recombination rate of photogenerated electron-hole pairs. The chemical state of active metals may be beneficial to the improving photocatalytic activity for CO<sub>2</sub> conversion with H<sub>2</sub>O.

#### 3.5. The results of UV-vis diffuse reflectance spectroscopy (DRS)

The optical absorption properties of TiO<sub>2</sub> nanocrystal, Pt/TiO<sub>2</sub>, Ru/TiO<sub>2</sub> and PtRu/TiO<sub>2</sub> catalysts were investigated by means of UV-vis DRS, and the result is shown in Fig. 6. In order to comparison, the commercial P25 is also included. Anatase TiO<sub>2</sub> nanocrystal with coexposed facets of {001} and {101} shows the stronger absorption intensity in visible range than commercial P25 with limited visible light adsorption. It is attributed to the existence of surface oxygen defects due to the presence of enlarged Ti-O-Ti bond angles and abundant coordination unsaturated Ti atoms on the {001} facet of anatase TiO<sub>2</sub> nanocrystals [52]. In our previous work [53], the visible absorption relationship between the origin and an oxygen defects on the {001} facet of TiO<sub>2</sub> nanocrystal are elucidated by DFT calculation on the surface density of states (DOS). TiO<sub>2</sub> nanocrystal with an oxygen vacancy (TiO<sub>2-x</sub>) needs lower energy to excite photogenerated electrons from valence band to conduction band, indicating that the photons in visible region can be absorbed by TiO<sub>2-x</sub>. For Pt/TiO<sub>2</sub> catalyst, it shows the stronger visible light absorption intensity and exhibits a slight red shift of absorption edge in comparison with anatase TiO<sub>2</sub> nanocrystal, which is attributed to the localized surface plasmon resonance effect of supported Pt NPs on enhanced light-trapping efficiency [54]. After introduction of supported Ru NPs, the visible light absorption intensity of Ru/TiO<sub>2</sub> catalyst is improved obviously, indicating that supported Ru NPs can enhance the visible light absorption efficiency. For PtRu/TiO<sub>2</sub> catalyst, the absorption intensity for visible light is lower than that of Ru/TiO<sub>2</sub> catalyst due to the decreasing amounts of Ru components. The band energy gaps of all catalysts could be calculated by the equation of  $(\alpha h\nu)^n = A(h\nu - Eg)$ , where  $\alpha$  is the absorption coefficient,  $h\nu$  is the absorption energy,  $A$  is the parameter that related to the effective masses associated with the valence and conduction bands,  $n$  is 1/2 for a direct transition and  $Eg$  is the band gap energy [55]. Fig. 6B shows the plotting  $(\alpha h\nu)^{1/2}$  versus  $h\nu$  according to the results of spectral response in Fig. 6A, and the extrapolated intercept of absorption edge tangent with x-axis corresponds to  $Eg$  values. It is noted that the  $Eg$  value (3.00 eV) of anatase TiO<sub>2</sub> nanocrystal is smaller than commercial P25 (3.20 eV). After introduction of Pt and Ru NPs, the  $Eg$  values decrease successively

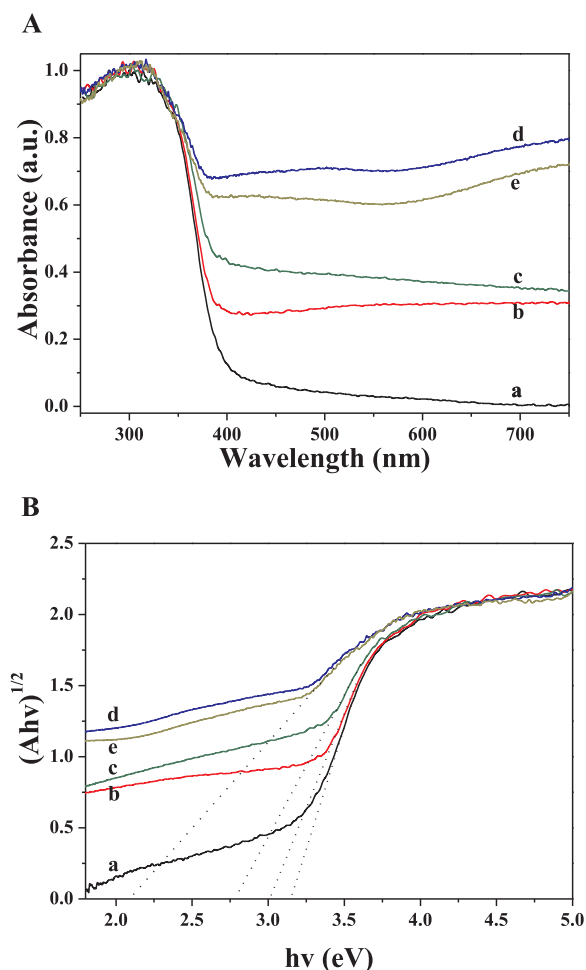


**Fig. 6.** UV-vis DRS (A) and Kubelka-Munk transformed reflectance spectra (B) of P25 (a), TiO<sub>2</sub> (b), Pt/TiO<sub>2</sub> (c), Ru/TiO<sub>2</sub> (d) and PtRu/TiO<sub>2</sub> (e) catalysts.

to 2.78 and 2.05 eV, which is attribute to the additional absorption band of supported Pt and Ru NPs in the visible region. PtRu/TiO<sub>2</sub> catalyst also shows the narrow optical band gap energy (2.10 eV) due to the strong visible-light absorption band of supported PtRu NPs. Thus, PtRu/TiO<sub>2</sub> catalyst with enhanced visible-light absorption can be as a promising photocatalyst for CO<sub>2</sub> conversion with H<sub>2</sub>O.

### 3.6. The results of photoluminescence (PL) spectra

PL emission spectroscopy is quite helpful to investigate the separation and migration efficiency of photogenerated electron-hole pairs in semiconductor photocatalysts. The intensity of PL emission spectrum can explore the recombination efficiency of photogenerated electron-hole pairs, and the low intensity of PL spectrum can reflect to the low recombination efficiency of photogenerated electron-hole pairs. In other words, the lower PL intensity is, the higher separation efficiency is. PL emission spectra of TiO<sub>2</sub> nanocrystal, Pt/TiO<sub>2</sub>, Ru/TiO<sub>2</sub> and PtRu/TiO<sub>2</sub> catalysts were carried out by using the excitation wavelength ( $\lambda_{Ex}$ ) of 380 nm, and the results are shown in Fig. 7. In order to comparison, the PL spectrum of commercial P25 is also included. The emission peak centered at 370–600 nm is assigned to the recombination of photogenerated electrons and holes. Anatase TiO<sub>2</sub> nanocrystal shows the lower intensity of PL emission spectrum in comparison with commercial P25. It indicates that the transfer and separation efficiency of photogenerated electrons and holes can be improved by the surface heterojunction of single anatase TiO<sub>2</sub> nanocrystal with coexposed {001} and {101} facets. After introduction of supported Pt and Ru NPs,

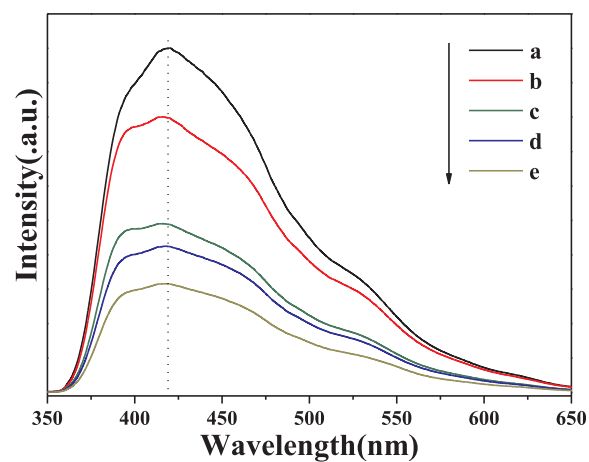


**Fig. 7.** Photoluminescence spectra ( $\lambda_{Ex}$  = 380 nm) of P25 (a), TiO<sub>2</sub> (b), Pt/TiO<sub>2</sub> (c), Ru/TiO<sub>2</sub> (d) and PtRu/TiO<sub>2</sub> (e) catalysts.

the intensities of PL emission spectra decrease successively, indicating that the Pt(Ru)-TiO<sub>2</sub> nanojunctions can suppress the recombination rate of photogenerated electron-hole pairs and extend the fate of photo-generated electrons. Among the catalysts, PtRu/TiO<sub>2</sub> catalyst exhibits the lowest intensity of PL emission spectra, suggesting that the synergic effect between Pt and Ru in Pt-Ru alloy NPs can increase the separation efficiency of photogenerated electrons and holes, which is favorable to improving the photocatalytic activity for CO<sub>2</sub> reduction with H<sub>2</sub>O.

### 3.7. The results of transient photocurrent response characterization

It is generally accepted that the photocatalytic activity for CO<sub>2</sub> conversion depends strongly on the enrichment degree of photogenerated electrons and holes on the surface of photocatalysts, which can be investigated by the transient photocurrent response using the incident light induced [56]. The higher photocurrent response intensity is, the larger photogenerated carrier density on the surface of catalyst is [57]. In order to further investigate the property of supported Pt and Ru NPs for promoting separation efficiency of photogenerated electron-hole pairs, the transient photocurrent responses were performed by using several on/off cycles of UV-vis light irradiation, and the results are showed in Fig. 8. The photocurrent intensity increased immediately with turning on the light irradiation, while it rapidly decreased to zero with turning off the light. It is worth noted that the photocurrent intensity of anatase TiO<sub>2</sub> nanocrystal is higher than that of commercial P25, indicating that the surface heterojunction effect between {001} and {101} facets can improve the relatively surface enrichment degree of photogenerated electrons. After introduction of Pt and Ru NPs, the

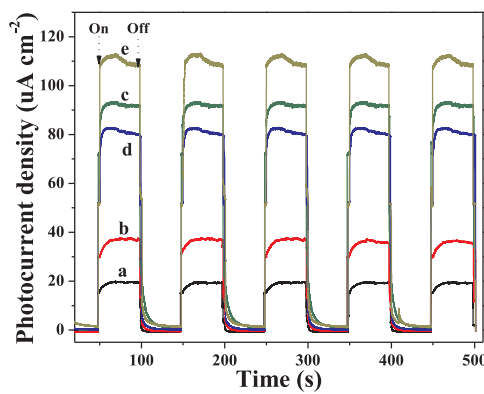


**Fig. 8.** Transient photocurrent responses of P25 (a), TiO<sub>2</sub> (b), Pt/TiO<sub>2</sub> (c), Ru/TiO<sub>2</sub> (d) and PtRu/TiO<sub>2</sub> (e) catalysts.

transient photocurrent intensities are higher than that of anatase TiO<sub>2</sub> nanocrystal, indicating that supported Pt and Ru NPs can further improve the separation and transfer efficiency of photogenerated electrons and holes. PtRu/TiO<sub>2</sub> catalyst shows the highest intensity of transient photocurrent response, indicating that it has the most separation efficiency of photogenerated electron-hole pairs and the highest surface enrichment degree of photogenerated electrons, which is in accordance with the result of PL emission spectra. In addition, during five turning on/off cycles of light irradiation, all catalysts display a relatively stable photocurrent response, suggesting the good stability of photogenerated charges separation. The enhanced separation efficiency of photogenerated electrons and holes over supported PtRu catalysts will highlight the excellent photocatalytic performance for CO<sub>2</sub> reduction with H<sub>2</sub>O.

### 3.8. The results of CO<sub>2</sub>-TPD and H<sub>2</sub>-TPD characterizations

The reaction nature of photocatalytic CO<sub>2</sub> reduction with H<sub>2</sub>O is a heterogeneous catalysis occurring at the interface between solid (catalytic) and gas (CO<sub>2</sub>), thus, the adsorption and activation for gas reactants are crucial to improve photocatalytic activity for CO<sub>2</sub> conversion. The adsorption/desorption properties for CO<sub>2</sub> and H<sub>2</sub> reactants are investigated by temperature-programmed desorption of CO<sub>2</sub> (CO<sub>2</sub>-TPD) and H<sub>2</sub> (H<sub>2</sub>-TPD) experiments, and the results are shown in Fig. 9. As shown in Fig. 9A, commercial P25 as a reference shows relatively weak desorption peak of CO<sub>2</sub>. The intensity of CO<sub>2</sub> desorption peak over anatase TiO<sub>2</sub> nanocrystal is stronger obviously than that of commercial P25, which is attributed to the increasing adsorption capacity on the surface of {001} facet with high surface energy. After supported Pt, Ru and Pt-Ru NPs on the surface of anatase TiO<sub>2</sub> nanocrystal, the intensities of CO<sub>2</sub> desorption peaks further increase, and Ru/TiO<sub>2</sub> catalyst shows the largest CO<sub>2</sub> desorption peaks, indicating that supported noble metal NPs can increase the adsorption capacity for CO<sub>2</sub> reactant, especially supported Ru NPs. The desorption peaks of CO<sub>2</sub> in the range of 70–180 and 180–350 °C are assigned to the strong physical adsorption and the weak chemical adsorption on the surface of supported noble metal NPs, respectively. The intensity of CO<sub>2</sub> desorption peak over supported PtRu NP catalyst with loading amount of Ru (1.9 wt%) is similar to that of Ru/TiO<sub>2</sub> catalyst with loading amount of Ru (3.7 wt %), indicating that the synergic effect of Pt and Ru components in bimetallic PtRu alloy NPs can increase the adsorption capacity for CO<sub>2</sub> reactant. As shown in Fig. 9B, there is a main desorption peak of H<sub>2</sub> centered at 130 °C and a shoulder peak centered at 180 °C, which are assigned to the strong physical adsorption and the weak chemical adsorption for H<sub>2</sub>, respectively. And anatase TiO<sub>2</sub> nanocrystal shows the relatively bigger desorption peak of H<sub>2</sub> than commercial P25, indicating that the co-exposed {001} and {101} facets with high surface energy can improve the adsorption property for H<sub>2</sub>. After introduction of

supported Pt, Ru and Pt-Ru NPs, the intensities of H<sub>2</sub> desorption peaks further increase remarkably, suggesting that supported noble metal NPs have good adsorption and activation properties for H<sub>2</sub>, which is beneficial to improve the selectivity of H-containing products for photocatalytic CO<sub>2</sub> reduction. Among the prepared catalysts, Pt/TiO<sub>2</sub> catalyst shows the highest intensity of H<sub>2</sub> desorption peak, and the temperature range of supported PtRu NP catalyst is widest, indicating that H<sub>2</sub> adsorption capacity or hydrogen proton enrichment is dependent on supported Pt NPs and it can be improved by the synergic effect of Pt and Ru components in bimetallic PtRu alloy NPs. Based on the results of characterizations, PtRu/TiO<sub>2</sub> catalyst, combined of both excellent photogenerated charges separation efficiency and strong adsorption capacities for CO<sub>2</sub> and H<sub>2</sub>, is promising to exhibit the high photocatalytic activity for CO<sub>2</sub> conversion with H<sub>2</sub>O to hydrocarbon fuels.

### 3.9. Photocatalytic performances for CO<sub>2</sub> reduction with H<sub>2</sub>O

The photocatalytic performances of TiO<sub>2</sub> nanocrystal, Pt/TiO<sub>2</sub>, Ru/TiO<sub>2</sub> and PtRu/TiO<sub>2</sub> catalysts for CO<sub>2</sub> conversion with H<sub>2</sub>O were carried out in a gas-closed circulation system under the simulated light irradiation with wavelength of 320–780 nm, and the evolution amounts of CH<sub>4</sub>, CO and H<sub>2</sub> products and the selectivity of CO<sub>2</sub> conversion are shown in Fig. 10 and Table 3. The catalytic performance for photocatalytic CO<sub>2</sub> reduction over commercial P25 as reference catalyst is also included. As shown in Fig. 10a, the amount of CH<sub>4</sub> product over anatase TiO<sub>2</sub> nanocrystal is larger than that of commercial P25. It is attributed to that the surface heterojunction between coexposed {101} and {001} facets in single anatase TiO<sub>2</sub> nanocrystal can improve the separation efficiency of photogenerated electrons and holes. After supported Pt and Ru NPs, the amounts of CH<sub>4</sub> product increase obviously, i.e., the formation rates of CH<sub>4</sub> over Pt/TiO<sub>2</sub> and Ru/TiO<sub>2</sub> catalysts increase to 22.9 and 9.7 μmol g<sup>-1</sup> h<sup>-1</sup> in Table 3, which are 17 and 7-fold of commercial P25, respectively. It is attributed to increasing the surface photogenerated electron density trapped by supported Pt and Ru NPs with the low Fermi energy level, which is beneficial to improve the formation of CH<sub>4</sub>. Among the as-prepared catalysts, PtRu/TiO<sub>2</sub> catalyst shows the highest formation rate of CH<sub>4</sub> (38.7 μmol g<sup>-1</sup> h<sup>-1</sup>), which is a 29-fold increase in comparison with commercial P25. It indicates that the noticeable synergistic effect of Pt and Ru components can enhance the photocatalytic performance for CO<sub>2</sub> conversion with H<sub>2</sub>O to CH<sub>4</sub>.

CO is also an important product of photocatalytic CO<sub>2</sub> conversion. Fig. 10b shows the amounts of CO product over all the catalysts. It is worth noted that Ru/TiO<sub>2</sub> catalyst shows the highest formation rate of CO product (18.1 μmol g<sup>-1</sup> h<sup>-1</sup>) in Table 3, and Pt/TiO<sub>2</sub> catalyst shows the lowest formation rate of CO product (1.3 μmol g<sup>-1</sup> h<sup>-1</sup>). It is also generally known that photocatalytic reduction of CO<sub>2</sub> to CH<sub>4</sub> and CO takes place companying with the reduction of H<sub>2</sub>O to H<sub>2</sub>. Thus, H<sub>2</sub> is an

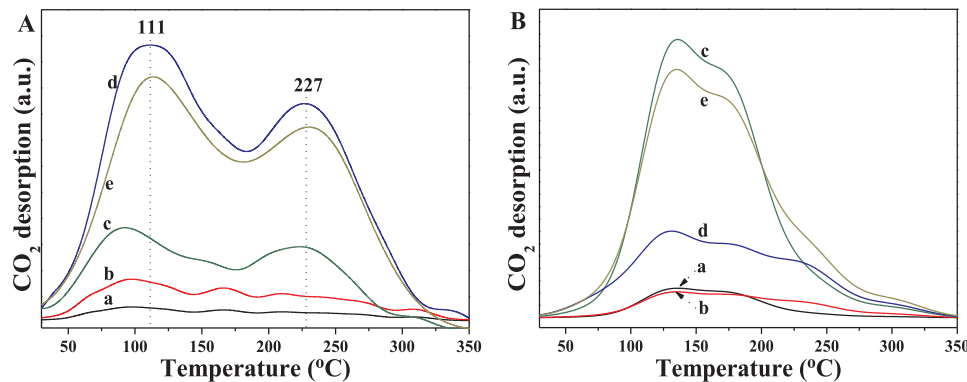


**Fig. 9.** Temperature-programmed desorption curves of CO<sub>2</sub> (CO<sub>2</sub>-TPD, A) and H<sub>2</sub> (H<sub>2</sub>-TPD, B) curves of P25 (a), TiO<sub>2</sub> (b), Pt/TiO<sub>2</sub> (c), Ru/TiO<sub>2</sub> (d) and PtRu/TiO<sub>2</sub> (e) catalysts.

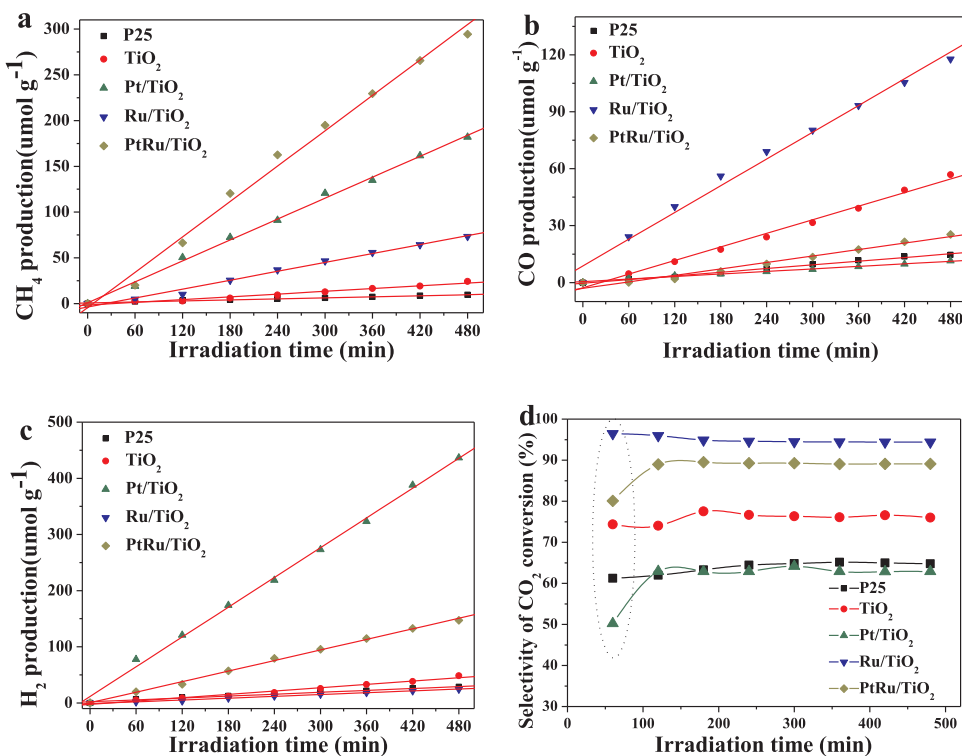


Fig. 10. Evolutions of CH<sub>4</sub> (a), CO (b), H<sub>2</sub> (c) products and the selectivity of CO<sub>2</sub> conversion (d) for photocatalytic conversion of CO<sub>2</sub> with H<sub>2</sub>O over P25, TiO<sub>2</sub>, Pt/TiO<sub>2</sub>, Ru/TiO<sub>2</sub> and PtRu/TiO<sub>2</sub> catalysts.

important by-product of photocatalytic CO<sub>2</sub> conversion with H<sub>2</sub>O. Fig. 10c shows the amounts of H<sub>2</sub> product over all the catalysts. In contrast to the formation rate of CO product, Pt/TiO<sub>2</sub> catalyst shows the highest formation rate of H<sub>2</sub> product (52.8 μmol g<sup>-1</sup> h<sup>-1</sup>), while Ru/TiO<sub>2</sub> catalyst exhibits the lowest formation rate of H<sub>2</sub> product (3.2 μmol g<sup>-1</sup> h<sup>-1</sup>). It suggests that the catalytic mechanism of supported Ru NP catalyst is different from supported Pt NP catalyst. Supported Ru NPs are favorable for improving the formation rate of CO product, and supported Pt NPs prefers to enhance the formation rate of CH<sub>4</sub> and H<sub>2</sub> products, which is related to the characters of trapping electrons and hydrogen protons over supported Pt NPs and the adsorption property of supported Ru NPs for CO<sub>2</sub> reactant. PtRu/TiO<sub>2</sub> catalyst can further improve the formation rates of CO and CH<sub>4</sub> in comparison with Pt/TiO<sub>2</sub> and Ru/TiO<sub>2</sub> catalyst, respectively. It indicates that the synergic effect between Pt and Ru components in supported Pt-Ru NPs can enhance the photocatalytic CO<sub>2</sub> conversion with H<sub>2</sub>O to CH<sub>4</sub> and CO.

Considering that the photocatalytic H<sub>2</sub>O reduction to H<sub>2</sub> is a

competitive reaction with the photocatalytic CO<sub>2</sub> reduction to CH<sub>4</sub> and CO,[58] the selectivity for CO<sub>2</sub> reduction was evaluated by the equation as listed of 2.3 section, and the results are shown in Fig. 10d. Ru/TiO<sub>2</sub> catalyst shows the highest selectivity for CO<sub>2</sub> reduction (94.7% in Table 3) rather than H<sub>2</sub>O reduction, and that of Pt/TiO<sub>2</sub> catalyst is the lowest (63.8% in Table 3). It indicates that the photogenerated electrons trapped by supported Pt NPs are not only used to CO<sub>2</sub> reduction, but also are used to H<sub>2</sub>O reduction to H<sub>2</sub> for the reaction process of two electrons consumption, while the photogenerated electrons trapped by supported Ru NPs are mainly applied to CO<sub>2</sub> reduction to CO (major) and CH<sub>4</sub> (secondary). Based on the results of transient photocurrent responses, CO<sub>2</sub>-TPD and H<sub>2</sub>-TPD, one speculation is reasonable that in the process of photocatalytic reduction of CO<sub>2</sub> with H<sub>2</sub>O, the surface concentration of CO<sub>2</sub> over supported Pt catalyst is not enough to completely consume the photogenerated electron, and the trapping photogenerated electrons over supported Ru catalyst is not enough to achieve the CO<sub>2</sub> conversion to CH<sub>4</sub>. Supported bimetallic Pt-Ru alloy NPs can not only improve the surface density of CO<sub>2</sub> but also increase

Table 3

The formation rates, the selectivity of CO and CH<sub>4</sub> productions and the apparent quantum efficiency (AQE) for photocatalytic conversion of CO<sub>2</sub> with H<sub>2</sub>O over P25, TiO<sub>2</sub>, Pt/TiO<sub>2</sub>, Ru/TiO<sub>2</sub> and PtRu/TiO<sub>2</sub> catalysts.

Sample	Formation rate [μmol g <sup>-1</sup> h <sup>-1</sup> ] <sup>a</sup>				S <sub>CO<sub>2</sub></sub> (%) <sup>b</sup>	S <sub>CH<sub>4</sub></sub> (%) <sup>c</sup>	S <sub>CO</sub> (%) <sup>c</sup>	AQE Φ (%) <sup>d</sup>
	CH <sub>4</sub>	CO	H <sub>2</sub>	O <sub>2</sub>				
P25	1.3	1.8	3.8	N.d. <sup>e</sup>	64.8	41.9	58.1	0.06
TiO <sub>2</sub>	3.0	7.2	5.9	16.3	76.5	29.4	70.6	0.15
Pt/TiO <sub>2</sub>	22.9	1.3	52.8	78.2	63.8	94.6	5.4	0.67
Ru/TiO <sub>2</sub>	9.7	18.1	3.2	41.1	94.7	34.9	65.1	0.48
PtRu/TiO <sub>2</sub>	38.7	2.6	16.5	102.7	90.5	93.7	6.3	0.98

<sup>a</sup> Reaction conditions: photocatalyst, 0.1 g; CO<sub>2</sub> pressure, 0.1 MPa; H<sub>2</sub>O, 2.0 mL; light source, 320–780 nm; irradiation time, 8 h; reaction temperature, 4 °C.

<sup>b</sup> The selectivity of CO<sub>2</sub> reduction (S<sub>CO<sub>2</sub></sub>) was evaluated by equation in section of 2.3.

<sup>c</sup> The selectivity to CH<sub>4</sub> (S<sub>CH<sub>4</sub></sub>) and CO (S<sub>CO</sub>) products from CO<sub>2</sub> reduction are obtained by the ratios of [CO] or [CH<sub>4</sub>] amounts to sum ([CO] + [CH<sub>4</sub>]) amounts.

<sup>d</sup> The apparent quantum efficiency with irradiation light of 380 nm.

<sup>e</sup> Not determined.

the trapping photogenerated electrons, thus, PtRu/TiO<sub>2</sub> catalyst with the synergic effect of Pt and Ru components shows high the selectivity for CO<sub>2</sub> reduction (90.5% in Table 3).

The selectivities of CH<sub>4</sub> and CO as two main products of CO<sub>2</sub> reduction were also investigated, and the result is shown in Table 3. Compared with commercial P25, TiO<sub>2</sub> nanocrystal shows the higher selectivity to CO product and the lower selectivity to CH<sub>4</sub> product, which may be attributed to the low enrichment degree of photogenerated electrons on the {101} facet of TiO<sub>2</sub> nanocrystal. After introduction of supported Pt and Ru NPs, Pt/TiO<sub>2</sub> catalyst shows the highest selectivity of CO<sub>2</sub> reduction to CH<sub>4</sub> product (94.6%), while the selectivity of CO<sub>2</sub> reduction to CH<sub>4</sub> product over Ru/TiO<sub>2</sub> catalyst is just only 34.9%. It indicates that supported Pt NPs can improve the surface density of photogenerated electrons originated from the excited TiO<sub>2</sub> nanocrystal, and the role of supported Ru NPs can increase the adsorption capacity for CO<sub>2</sub> reactant. PtRu/TiO<sub>2</sub> catalyst with the synergic effect of Pt and Ru components, which combines of both the high enrichment density of photogenerated electrons by Pt component and the strong adsorption capacity for CO<sub>2</sub> by Ru component, shows significantly improving photocatalytic selectivity for CO<sub>2</sub> reduction with H<sub>2</sub>O to CH<sub>4</sub> (93.7%) rather than CO and H<sub>2</sub>. In addition, the formation rate of O<sub>2</sub> as the main product of photogenerated holes consumption reaction is an important factor to investigate the conservation of chemical reaction mass. Table 3 shows the formation rates of O<sub>2</sub> over the as-prepared catalysts. Among all the catalysts, PtRu/TiO<sub>2</sub> catalyst shows the highest formation rate of O<sub>2</sub> product (102.7 μmol g<sup>-1</sup> h<sup>-1</sup>), which is higher than the stoichiometric rate according to the calculation of CH<sub>4</sub>, CO and H<sub>2</sub> products (87.0 μmol g<sup>-1</sup> h<sup>-1</sup>). It indicates that other hydrocarbon products may be formed and undetected, which is an important research point to discovery and investigation of other hydrocarbons in the future.

The apparent quantum efficiency (AQE) of the photocatalysts for CO<sub>2</sub> reduction with H<sub>2</sub>O is the most important parameter to investigate light-chemical energy conversion. For the photocatalytic reaction of CO<sub>2</sub> conversion with H<sub>2</sub>O, the AQE values for CH<sub>4</sub> and CO products over TiO<sub>2</sub> nanocrystal, Pt/TiO<sub>2</sub>, Ru/TiO<sub>2</sub> and PtRu/TiO<sub>2</sub> catalysts were calculated by the equation as listed of 2.3 section, and the results are listed in Table 3. The AQE value of anatase TiO<sub>2</sub> nanocrystal (0.15%) is obviously higher than that of commercial P25 (0.06%), which is attributed to the enhanced separation efficiency of photogenerated electron-hole pairs due to the surface heterojunction between coexposed {001} and {101} facets. After supported Pt and Ru NPs, the AQE values of Pt/TiO<sub>2</sub> and Ru/TiO<sub>2</sub> catalysts increase to 0.65 and 0.48%, which is attributed to increase the enrichment density of photogenerated electrons and the adsorption capacity for CO<sub>2</sub>, respectively. PtRu/TiO<sub>2</sub> catalyst exhibits the largest AQE value (0.98%). It is further confirmed that the synergic effect of Pt and Ru components in supported bimetallic Pt-Ru alloy NPs is beneficial to improve the utilization efficiency of simulated solar irradiation.

The catalytic stability of PtRu/TiO<sub>2</sub> photocatalyst for CO<sub>2</sub> reduction with H<sub>2</sub>O was investigated by the five-cycle tests under same condition of light irradiation, and the result is shown in Fig. 11. PtRu/TiO<sub>2</sub> photocatalyst exhibits good activity stability for CO<sub>2</sub> reduction, i.e., the formation rates of H<sub>2</sub>, CH<sub>4</sub> and CO products have not changed obviously during the five cycles. Based on the TEM image of PtRu/TiO<sub>2</sub> catalyst used five cycles (Fig. S5), the nanostructure and particle sizes of supported bimetallic PtRu alloy NPs selectively deposited on {101} facet of anatase TiO<sub>2</sub> nanocrystal have not changed obviously, indicating that the photocatalysts have good catalytic and structured stability. It suggests that PtRu/TiO<sub>2</sub> photocatalyst has a strong application potential in CO<sub>2</sub> reduction with H<sub>2</sub>O.

In addition, in order to illustrate the carbon and hydrogen sources in CH<sub>4</sub> and CO products, a series of background experiments and isotopic tracing of <sup>13</sup>C and <sup>2</sup>H(D) were also performed. For blank test without photocatalyst, no product of CO<sub>2</sub> conversion with H<sub>2</sub>O was observed although using the same condition of simulated light irradiation,

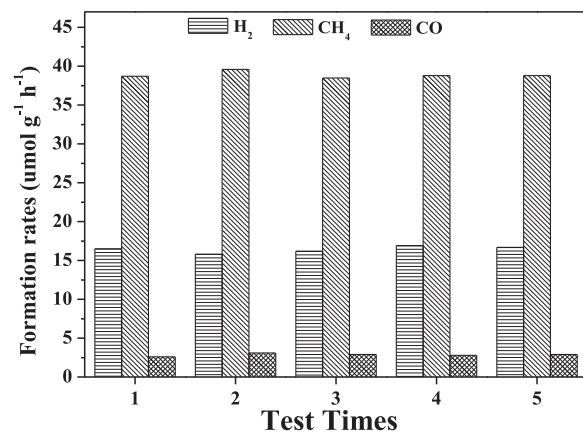


Fig. 11. Stability investigation on the formation rate of products (CH<sub>4</sub>, CO and H<sub>2</sub>) over PtRu/TiO<sub>2</sub> catalyst for five test cycles.

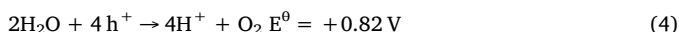
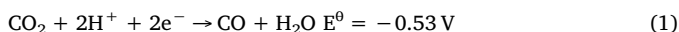
indicating that the photocatalytic reaction of CO<sub>2</sub> reduction depends on the present of photocatalyst. The other experiment was carried out under condition of without light irradiation, any product over PtRu/TiO<sub>2</sub> photocatalyst was not observed, indicating that the photocatalytic reaction of CO<sub>2</sub> reduction depends on the light irradiation. One more experiment using PtRu/TiO<sub>2</sub> catalyst and simulated light irradiation with the reactant gases of N<sub>2</sub> and H<sub>2</sub>O was performed, and again, the carbon-containing products (CO and CH<sub>4</sub>) were not detected, indicating that the carbon in CO and CH<sub>4</sub> products come from CO<sub>2</sub> reactant. In order to direct verify the sources of carbon and hydrogen in the products, the isotopic tracings of <sup>13</sup>C and <sup>2</sup>H(D) in photocatalytic <sup>13</sup>C-labeled CO<sub>2</sub> reduction with D<sub>2</sub>O over PtRu/TiO<sub>2</sub> catalyst were performed by means of GC-MS after 8 h light irradiation, and the result is shown in Fig. S6. The m/z signal at 21 can be attributed to <sup>13</sup>CD<sub>4</sub>, and the m/z signal at 29 can be assigned as <sup>13</sup>CO. It is direct proof that the carbon element in the product of CO and CH<sub>4</sub> originates from CO<sub>2</sub> reactant, and the hydrogen element in the product of CH<sub>4</sub> originates from H<sub>2</sub>O reactant. Therefore, it is asserted that CO<sub>2</sub> and H<sub>2</sub>O reactants are only source to the products (CO and CH<sub>4</sub>) of photocatalytic CO<sub>2</sub> reduction with H<sub>2</sub>O, and both photocatalysts and light irradiation are also necessary.

### 3.10. Discussion on the mechanism of PtRu/TiO<sub>2</sub> catalyst for CO<sub>2</sub> reduction with H<sub>2</sub>O

The nature of photocatalytic CO<sub>2</sub> reduction with H<sub>2</sub>O under light irradiation is a solid (catalyst)-gas (CO<sub>2</sub> and H<sub>2</sub>O) heterogeneous catalysis reaction derived by photogenerated charges. Thus, the catalytic performance of photocatalysts for CO<sub>2</sub> reduction is dependent on their semi-conductor characters and the adsorption/activation property for CO<sub>2</sub> and H<sub>2</sub>O reactants. The architecture of nanostructured semiconductor with surface-decorated noble metal NPs is usually utilized in the most efficient photocatalytic systems.[59] The photocatalysts with coupling semiconductors and metal NPs are beneficial for the enhancing photocatalytic performance for CO<sub>2</sub> reduction via the optimizing governing factors including improved charge separation, facilitated CO<sub>2</sub> activation and additional active sites. Thus, the discussion on the mechanism of PtRu/TiO<sub>2</sub> photocatalyst for CO<sub>2</sub> reduction can be isolated from the charge-separation functions and the adsorption/activation property for CO<sub>2</sub> and H<sub>2</sub>O reactants.

It is well known that the efficient photocatalysts for CO<sub>2</sub> reduction to CO and CH<sub>4</sub> must be confirmed by the energy band theory, which is based on the positions of conduction band (CB), valence band (VB) of photocatalysts and reduction potentials of reactions. When the reduction potential of the reaction is lower than the CB position of the photocatalysts, photogenerated electrons on the surface of photocatalyst can be consumed effectively. During the process of

photocatalytic  $\text{CO}_2$  with  $\text{H}_2\text{O}$ , the possible reactions can be described by the thermodynamic reduction potentials versus normal hydrogen electrode (NHE) and the equations in (1)–(4) [60].



The CB potential ( $E_{\text{CB}}$ ) of  $\text{TiO}_2$  (-0.56 V vs. NHE at pH 7) as the foundation of photogenerated electrons is more negative than the reduction potentials of  $E^\theta(\text{CO}_2/\text{CO})$  (-0.53 V) and  $E^\theta(\text{CO}_2/\text{CH}_4)$  (-0.24 V), indicating that the reactions for photocatalytic  $\text{CO}_2$  reduction to CO and  $\text{CH}_4$  products are theoretically feasible. As shown in equations (1) and (2), eight electrons and eight hydrogen protons are required to produce  $\text{CH}_4$  in comparison with only two electrons and two hydrogen protons for CO product, although the  $E^\theta(\text{CO}_2/\text{CH}_4)$  is less negative than  $E^\theta(\text{CO}_2/\text{CO})$ . So the CO product is possible to be priority under situation of the low surface density of photogenerated electrons and hydrogen protons. And the competitive reaction of  $\text{H}_2\text{O}$  reduction to  $\text{H}_2$  product can also be drove by the photogenerated electrons of  $\text{TiO}_2$  based on the lower reduction potential difference (-0.41 V). For anatase  $\text{TiO}_2$  nanocrystal photocatalyst, the surface heterojunction between coexposed {101} and {001} facets can be formed due to the directional migration of photogenerated carriers, which is beneficial to improve separation efficiency of photogenerated electron-hole pairs and change the CB and VB positions of anatase  $\text{TiO}_2$  nanocrystal reported by Yu [61] and Huang [62]. In order to investigate the CB position of PtRu/ $\text{TiO}_2$  catalyst, the density functional theory (DFT) calculation was performed by using the VASP code with the cutoff; energy of 400 eV and the DFT + U(4.2 eV) method, and the model for PtRu NPs supported on the surface of  $\text{TiO}_2$ –{101} facet is shown in Fig. S7. The  $E_{\text{CB}}$  values of anatase  $\text{TiO}_2$  nanocrystal and PtRu/ $\text{TiO}_2$  photocatalysts are -0.60 V and -0.71 V, respectively, which are more negative than the  $E_{\text{CB}}$  value of conventional  $\text{TiO}_2$  (-0.56 V vs. NHE at pH 7). Combined with the  $E^\theta$  values of the (1)–(4) equations, it indicates that the products of  $\text{H}_2$ , CO and  $\text{CH}_4$  derived from  $\text{H}_2\text{O}$  splitting and photocatalytic  $\text{CO}_2$  reduction should be detected, and the photocatalytic reactions over PtRu/ $\text{TiO}_2$  photocatalyst are easier than that over conventional  $\text{TiO}_2$  photocatalyst in theory. Therefore, the selectivity for photocatalytic  $\text{CO}_2$  reduction with  $\text{H}_2\text{O}$  to  $\text{H}_2$ , CO and  $\text{CH}_4$  products are strongly dependent on the surface density of photogenerated electrons, hydrogen protons and activated  $\text{CO}_2$ , in other words, the surface density of active species can change the evolution rules of  $\text{H}_2$ , CO and  $\text{CH}_4$  products via the optimized nanostructure and composition of photocatalysts.

For the photocatalytic process of  $\text{CO}_2$  reduction with  $\text{H}_2\text{O}$ , it can be summarized into three elemental steps: firstly, photogenerated carriers (electron-hole pairs) are formed by a band-gap excitation; secondly, the charge carriers are separated and enriched on the surface of catalyst; finally,  $\text{CO}_2$  and  $\text{H}_2\text{O}$  adsorbed on the surface of catalysts are reduced by photogenerated electrons. Thus, the enhanced photocatalytic activity for  $\text{CO}_2$  conversion with  $\text{H}_2\text{O}$  is dependent on the light-harvesting, the adsorption and activation for  $\text{CO}_2$ , and the charge separation. For the enhancing light-harvesting efficiency, supported Pt, Ru and Pt-Ru NPs can improve the absorption for visible light proved by the UV-Vis DRS (Fig. 6). For enhancing adsorption capacity for  $\text{CO}_2$ , supported Ru NPs play the main role obtained by the results of  $\text{CO}_2$ -TPD (Fig. 9A), and the synergic effect of Pt and Ru components in bimetallic PtRu alloy NPs can further increase the adsorption capacity for  $\text{CO}_2$  reactant.

For improving separation efficiency of photogenerated charges, single nanocrystal of anatase  $\text{TiO}_2$  after absorbed photons are excited to produce electron-hole pairs, which are enriched on the surface of coexposed {101} and {001} facets, respectively. Based on the results of PL (Fig. 7) and transient photocurrent (Fig. 8), the coexposed {101} and

{001} facets of anatase  $\text{TiO}_2$  nanocrystal can form a surface heterojunction, which is beneficial to enhance separation of photogenerated electrons and holes. And then photogenerated electrons on the surface heterojunction of {101} facet can transfer rapidly to supported noble metal NPs, which is direct proved by the selective reduction and deposition of noble metal NPs on the surface of {101} facet during the light irradiation process of P-GBMR method (Fig. 2 and Fig. S3). Thus, it occurs to the vectorial electron transfer from  $\text{TiO}_2$  to Pt NPs. Combined the results of XPS spectra (Fig. 5) and PL spectra (Fig. 7), the increasing surface ionic ( $\text{Pt}^{4+}$  and  $\text{Ru}^{4+}$ ) species have strong capacity to capture the photogenerated electron from CB of  $\text{TiO}_2$ . Supported PtRu NPs in PtRu/ $\text{TiO}_2$  catalyst are used as an accumulator for electron transfer in  $\text{TiO}_2$ -PtRu binary system. Finally, the photogenerated electrons are enriched on the surface of supported PtRu NPs, and subsequently react with adsorbed/activated  $\text{CO}_2$  and  $\text{H}_2\text{O}$  to  $\text{H}_2$ , CO and  $\text{CH}_4$  products.

Based on the results of photocatalytic  $\text{CO}_2$  conversion with  $\text{H}_2\text{O}$  in Fig. 10 and Table 3, the role of supported Pt NPs is assigned to the trapping and enrichment of photogenerated electrons and hydrogen (H) protons proved by  $\text{H}_2$ -TPD, and the role of supported Ru NPs is assigned to the adsorption and activation for  $\text{CO}_2$  reactant. Thus, Pt/ $\text{TiO}_2$  catalyst with surface electron/H-rich and  $\text{CO}_2$ -lean characters prefers to increase the formation rates of  $\text{CH}_4$  and  $\text{H}_2$ , while Ru/ $\text{TiO}_2$  catalyst with surface properties of  $\text{CO}_2$ -rich and electron/H-lean is favorable for improving the formation rate of CO. And PtRu/ $\text{TiO}_2$  catalyst with the synergic effect between Pt and Ru components can improve obviously the selectivity for  $\text{CO}_2$  reduction and the formation rates of  $\text{CH}_4$  and CO. It is noted that, at the beginning stage of photocatalytic  $\text{CO}_2$  reduction with  $\text{H}_2\text{O}$  in Fig. 10d, the selectivities of  $\text{CO}_2$  conversion over Pt/ $\text{TiO}_2$  and PtRu/ $\text{TiO}_2$  catalysts are lower obviously than those of the later stage, indicating that the photogenerated electrons at initial stage of reaction were mainly consumed and reacted with hydrogen protons to  $\text{H}_2$  product, in other words,  $\text{H}_2$  product is a priority among the products of photocatalytic  $\text{CO}_2$  reduction with  $\text{H}_2\text{O}$ . Thus, it is rationalized that the formation of H-containing species ( $\text{H}_2$ ) is an important intermediate for promoting photocatalytic reduction of  $\text{CO}_2$  with  $\text{H}_2\text{O}$  to  $\text{CH}_4$ .

In order to verify the possible mechanism, Fig. 12 shows the formation rate and the selectivity of  $\text{CH}_4$  product over P25,  $\text{TiO}_2$ , Pt/ $\text{TiO}_2$ , Ru/ $\text{TiO}_2$  and PtRu/ $\text{TiO}_2$  catalysts under conditions of  $\text{CO}_2$  pressure (0.5 bar) and  $\text{H}_2$  pressure (0.5 bar). In comparison with the condition of only  $\text{CO}_2$  gas, the formation rate and the selectivity of  $\text{CH}_4$  product over P25,  $\text{TiO}_2$  and Ru/ $\text{TiO}_2$  catalysts increase obviously after introduction of  $\text{H}_2$  as reactant, for example, the formation rate of  $\text{CH}_4$  product over Ru/ $\text{TiO}_2$  catalyst increases to 2.7 times and its selectivity to  $\text{CH}_4$  product increases from 35% to 99%. But the formation rate and the selectivity of  $\text{CH}_4$  product over Pt/ $\text{TiO}_2$  and PtRu/ $\text{TiO}_2$  catalysts have not increased obviously after introduction of  $\text{H}_2$  as reactant. It indicates

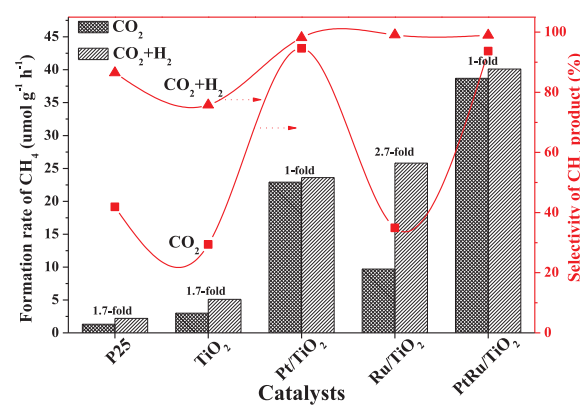
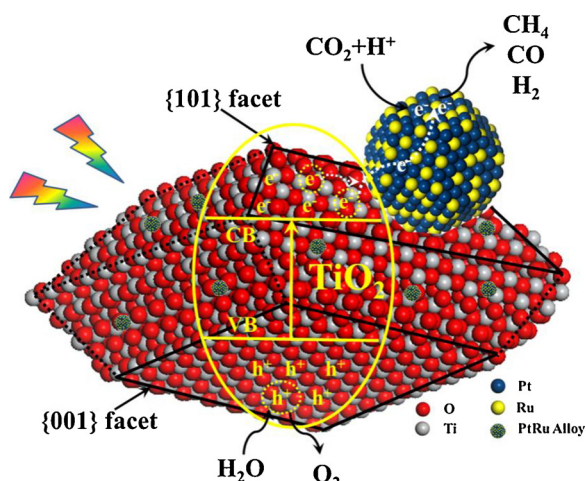


Fig. 12. The formation rate and the selectivity of  $\text{CH}_4$  product for photocatalytic conversion of  $\text{CO}_2$  with  $\text{H}_2\text{O}$  over P25,  $\text{TiO}_2$ , Pt/ $\text{TiO}_2$ , Ru/ $\text{TiO}_2$  and PtRu/ $\text{TiO}_2$  catalysts under conditions of  $\text{CO}_2$  pressure (1 bar) or  $\text{CO}_2$  pressure (0.5 bar) +  $\text{H}_2$  pressure (0.5 bar).



**Fig. 13.** Schematic of photocatalytic  $\text{CO}_2$  reduction with  $\text{H}_2\text{O}$  to  $\text{H}_2$ ,  $\text{CO}$  and  $\text{CH}_4$  products over  $\text{PtRu}/\text{TiO}_2$  catalyst.

that the formation of  $\text{H}_2$  as an intermediate is an important determining step for improving the formation rate and the selectivity of  $\text{CH}_4$  product in the photocatalytic reduction of  $\text{CO}_2$  with  $\text{H}_2\text{O}$ , and the catalytic performance of  $\text{Ru}/\text{TiO}_2$  catalyst is limited by the low supply rate of H-containing species compared with  $\text{Pt}/\text{TiO}_2$  catalyst.  $\text{PtRu}/\text{TiO}_2$  catalyst shows the synergic effect of surface electron/H-rich by Pt NPs and surface  $\text{CO}_2$ -rich by Ru NPs, which results in the high formation rate and selectivity of  $\text{CH}_4$  product.

Based on the discussion above, the photocatalytic mechanism for  $\text{CO}_2$  reduction with  $\text{H}_2\text{O}$  over  $\text{PtRu}/\text{TiO}_2$  catalyst is proposed and vividly shown in Fig. 13. For the  $\text{PtRu-TiO}_2$  ternary composites, anatase  $\text{TiO}_2$  nanocrystal with coexposed {001} and {101} facets is the fountainhead of photogenerated electrons which are enriched on the surface of {101} facets.  $\text{TiO}_2\text{-}\{001\}$  facet with high surface energies and enriched photogenerated holes can promote the oxidation reaction of  $\text{H}_2\text{O}$  to produce surface-bound hydrogen protons and  $\text{O}_2$  shown in equation (4). The surface heterojunction between coexposed {101} and {001} facets can improve the separation efficiency of photogenerated electrons and holes. Supported PtRu alloy NPs selectively deposited on the surface of  $\text{TiO}_2\text{-}\{101\}$  facet via P-GBMR method can gather photogenerated electrons from CB of anatase  $\text{TiO}_2$  nanocrystal, so photogenerated electrons are enrichment on the surface of PtRu NPs via the vectorial transfer of  $\text{TiO}_2\rightarrow\text{PtRu}$ . Meanwhile, Pt component in bimetallic Pt-Ru alloy NPs can further enrich the intermediate of H-containing species, and Ru component in bimetallic Pt-Ru alloy NPs is crucial to the adsorption and activation for  $\text{CO}_2$  reactant. Finally,  $\text{PtRu}/\text{TiO}_2$  catalyst with the synergic effect of Pt and Ru components shows the high formation rate and selectivity for photocatalytic  $\text{CO}_2$  reduction with  $\text{H}_2\text{O}$  to  $\text{CH}_4$  product. In summary, for the reaction of photocatalytic  $\text{CO}_2$  reduction with  $\text{H}_2\text{O}$ , the formation of H-containing intermediate and the activation for  $\text{CO}_2$  are two important determining steps for increasing the formation rate and the selectivity of  $\text{CH}_4$  product. The mechanism is reasonable explain that  $\text{PtRu}/\text{TiO}_2$  catalyst can solve the limitation of forming H-containing intermediate and activated  $\text{CO}_2$  for enhancing photocatalytic  $\text{CO}_2$  reduction with  $\text{H}_2\text{O}$  to  $\text{CH}_4$  product.

#### 4. Conclusions

We demonstrated a strategy to fabricate the novel photocatalyst of bimetallic PtRu alloy NPs selectively deposited on the {101} facet of  $\text{TiO}_2$  nanocrystal via the advanced synthetic processes of P-GBMR method. The surface heterojunction between coexposed {001}-61% and {101}-39% facets over anatase  $\text{TiO}_2$  nanocrystal can improve the separation efficiency of photogenerated electrons and holes, and the

photogenerated electrons are enriched on the surface of {101} facet. Supported noble metal NPs can further gather and enrich the photogenerated electrons via the vectorial transfer of  $\text{TiO}_2\rightarrow\text{PtRu}$ . Supported Pt catalyst with enriched photogenerated electrons shows the relative high formation rate of  $\text{CH}_4$  ( $22.9 \mu\text{mol g}^{-1} \text{h}^{-1}$ ) and  $\text{H}_2$  ( $52.8 \mu\text{mol g}^{-1} \text{h}^{-1}$ ), while supported Ru catalyst with strong activation for  $\text{CO}_2$  prefers to improve the selectivity to CO product (65.1%).  $\text{PtRu}/\text{TiO}_2$  catalyst with the synergic effect of Pt and Ru components shows the highest photocatalytic performances for  $\text{CO}_2$  reduction with  $\text{H}_2\text{O}$ . The possible mechanism of  $\text{PtRu}/\text{TiO}_2$  photocatalysts for  $\text{CO}_2$  reduction is proposed and discussed: the formation of H-containing intermediate and the activation for  $\text{CO}_2$  are two important determining steps for enhancing the photocatalytic  $\text{CO}_2$  reduction with  $\text{H}_2\text{O}$  to  $\text{CH}_4$  product.  $\text{PtRu}/\text{TiO}_2$  catalyst with the synergic effect of Pt and Ru components can solve the limitation of forming H-containing intermediate and activated  $\text{CO}_2$  for enhancing photocatalytic  $\text{CO}_2$  reduction with  $\text{H}_2\text{O}$  to  $\text{CH}_4$  product under simulated solar irradiation, i.e., its formation rate of  $\text{CH}_4$  ( $38.7 \mu\text{mol g}^{-1} \text{h}^{-1}$ ) is about 29-fold of commercial P25 and its apparent quantum efficiency for  $\text{CO}_2$  conversion is 0.98%. The design and fabrication of  $\text{PtRu}/\text{TiO}_2$  photocatalyst are expected to be a new heuristic on the development of high efficient photocatalysts for application to light-chemical energy conversion.

#### Acknowledgements

We acknowledge the financial support from the National Natural Science Foundation of China (21673142 and 21477164), National Engineering Laboratory for Mobile Source Emission Control Technology (NELMS2017A05) and Science Foundation of China University of Petroleum, Beijing (242017QNXZ02 and 2462018BJC005).

#### Appendix A. Supplementary data

Supplementary material related to this article can be found, in the online version, at doi:<https://doi.org/10.1016/j.apcatb.2018.05.043>.

#### References

- [1] K. Mori, T. Taga, H. Yamashita, ACS Catal. 7 (2017) 3147–3151.
- [2] A. Dhakshinamoorthy, S. Navalon, A. Corma, H. Garcia, Energy Environ. Sci. 5 (2012) 9217–9233.
- [3] X. Chang, T. Wang, J. Gong, Energy Environ. Sci. 7 (2016) 2177–2196.
- [4] E.V. Kondratenko, G. Mul, J. Baltrusaitis, G.O. Larrazábal, J. Pérez-Ramírez, Energy Environ. Sci. 6 (2013) 3122–3135.
- [5] Q. Kang, T. Wang, P. Li, L. Liu, K. Chang, M. Li, J. Ye, Angew. Chem. 127 (2015) 855–859.
- [6] T. Inoue, A. Fujishima, S. Konishi, K. Honda, Nature 277 (1979) 637–638.
- [7] S. Sato, T. Morikawa, T. Kajino, O. Ishitani, Angew. Chem. Int. Ed. 52 (2013) 988–992.
- [8] Y. Bai, L. Ye, T. Chen, P. Wang, L. Wang, X. Shi, P.K. Wong, Appl. Catal. B 203 (2017) 633–640.
- [9] H. Liu, T.D. Dao, L. Liu, X. Meng, T. Nagao, J. Ye, Appl. Catal. B 209 (2017) 183–189.
- [10] S. Wang, X. Wang, Angew. Chem. Int. Ed. 55 (2016) 2308–2320.
- [11] M. Anpo, H. Yamashita, K. Ikeue, Y. Fujii, S.G. Zhang, Y. Ichihashi, D.R. Park, Y. Suzuki, K. Koyano, T. Tatsumi, Catal. Today 44 (1998) 327–332.
- [12] X. She, J. Wu, H. Xu, Z. Mo, J. Lian, Y. Song, L. Liu, D. Du, H. Li, Appl. Catal. B 202 (2017) 112–117.
- [13] J. Qin, S. Wang, X. Wang, Appl. Catal. B 209 (2017) 476–482.
- [14] S. Wang, Y. Guan, L. Lu, Z. Shi, S. Yan, Z. Zou, Appl. Catal. B 224 (2018) 10–16.
- [15] L. Zhang, H. Fu, Y. Zhu, Adv. Funct. Mater. 18 (2008) 2180–2189.
- [16] T. Kamegawa, N. Suzuki, H. Yamashita, Energy Environ. Sci. 4 (2011) 1411–1416.
- [17] Y. Ma, X. Wang, Y. Jia, X. Chen, H. Han, C. Li, Chem. Rev. 114 (2014) 9987–10043.
- [18] Q. Zhang, T. Gao, J.M. Andino, Y. Li, Appl. Catal. B 123–124 (2012) 257–264.
- [19] Z. Bian, J. Zhu, J. Wen, F. Cao, Y. Huo, X. Qian, Y. Cao, M. Shen, H. Li, Y. Lu, Angew. Chem. Int. Ed. 50 (2011) 1105–1108.
- [20] X. Weng, Q. Zeng, Y. Zhang, F. Dong, Z. Wu, ACS Sustain. Chem. Eng. 4 (2016) 4314–4320.
- [21] Y. Wang, W. Yang, X. Chen, J. Wang, Y. Zhu, Appl. Catal. B 220 (2018) 337–347.
- [22] W.J. Ong, L.L. Tan, S.P. Chai, S.T. Yong, A.R. Mohamed, Nanoscale 6 (2014) 1946–2008.
- [23] T. Tachikawa, S. Yamashita, T. Majima, J. Am. Chem. Soc. 133 (2011) 7197–7204.
- [24] A. Meng, J. Zhang, D. Xu, B. Cheng, J. Yu, Appl. Catal. B 198 (2016) 286–294.
- [25] Y. Cao, Q. Li, C. Li, J. Li, J. Yang, Appl. Catal. B. 198 (2016) 378–388.

- [26] T. An, J. Chen, X. Nie, G. Li, H. Zhang, X. Liu, H. Zhao, *ACS Appl. Mater. Interfaces* 4 (2012) 5988–5996.
- [27] J. Jiao, Y. Wei, Z. Zhao, J. Liu, J. Li, A. Duan, G. Jiang, *Ind. Eng. Chem. Res.* 53 (2014) 17345–17354.
- [28] K. Zhang, Y. Liu, J. Deng, S. Xie, H. Lin, X. Zhao, J. Yang, Z. Han, H. Dai, *Appl. Catal. B* 202 (2017) 569–579.
- [29] X. Chen, Q. Chen, W. Jiang, Z. Wei, Y. Zhu, *Appl. Catal. B* 211 (2017) 106–113.
- [30] Y. Wei, J. Jiao, Z. Zhao, W. Zhong, J. Li, J. Liu, G. Jiang, A. Duan, *J. Mater. Chem. A* 3 (2015) 11074–11085.
- [31] Q. Zhai, S. Xie, W. Fan, Q. Zhang, Y. Wang, W. Deng, Y. Wang, *Angew. Chem. Int. Ed.* 52 (2013) 5776–5779.
- [32] B. Cao, G. Li, H. Li, *Appl. Catal. B* 194 (2016) 42–49.
- [33] Z. Zhang, S. Cao, Y. Liao, C. Xue, *Appl. Catal. B* 162 (2015) 204–209.
- [34] K. Ji, H. Dai, J. Deng, H. Zang, H. Arandiyani, S. Xie, H. Yang, *Appl. Catal. B* 168–169 (2015) 274–282.
- [35] Z. Xiong, Z. Lei, C.C. Kuang, X. Chen, B. Gong, Y. Zhao, J. Zhang, C. Zheng, *J.C.S. Wu*, *Appl. Catal. B* 202 (2017) 695–703.
- [36] F. Lin, D. Wang, Z. Jiang, Y. Ma, J. Li, R. Li, C. Li, *Energy Environ. Sci.* 5 (2012) 6400–6406.
- [37] F. Wang, Z. Jin, Y. Jiang, E.H.G. Backus, M. Bonn, S.N. Lou, D. Turchinovich, R. Amal, *Appl. Catal. B* 198 (2016) 25–31.
- [38] Y. Wang, J. Zhao, Y. Li, C. Wang, *Appl. Catal. B* 226 (2018) 544–553.
- [39] M. Wen, K. Mori, Y. Kuwahara, T. An, H. Yamashita, *Appl. Catal. B* 218 (2017) 555–569.
- [40] J. Ding, Y. Bu, M. Ou, Y. Yu, Q. Zhong, M. Fan, *Appl. Catal. B* 202 (2017) 314–325.
- [41] S. Xie, Y. Wang, Q. Zhang, W. Fan, W. Deng, Y. Wang, *Chem. Commun.* 49 (2013) 2451–2453.
- [42] K. Ohkubo, Y. Yamazaki, T. Nakashima, Y. Tamaki, K. Koike, O. Ishitani, *J. Catal.* 343 (2016) 278–289.
- [43] T.M. Suzuki, T. Takayama, S. Sato, A. Iwase, A. Kudo, T. Morikawa, *Appl. Catal. B* 224 (2018) 572–578.
- [44] Y. Wei, J. Liu, Z. Zhao, Y. Chen, C. Xu, A. Duan, G. Jiang, H. He, *Angew. Chem. Int. Ed.* 50 (2011) 2326–2329.
- [45] Y. Wei, Z. Zhao, J. Liu, S. Liu, C. Xu, A. Duan, G. Jiang, *J. Catal.* 317 (2014) 62–74.
- [46] H.G. Yang, C.H. Sun, S.Z. Qiao, J. Zou, G. Liu, S.C. Smith, H.M. Cheng, G.Q. Lu, *Nature* 453 (2008) 638–642.
- [47] J. Zhu, S. Wang, Z. Bian, S. Xie, C. Cai, J. Wang, H. Yang, H. Li, *CrystEngComm* 12 (2010) 2219.
- [48] J.G. Yu, J.X. Low, W. Xiao, P. Zhou, M. Jaroniec, *J. Am. Chem. Soc.* 136 (2014) 8839–8842.
- [49] J. Jiao, Y. Wei, Y. Zhao, Z. Zhao, A. Duan, J. Liu, Y. Pang, J. Li, G. Jiang, Y. Wang, *Appl. Catal. B* 209 (2017) 228–239.
- [50] F. Tian, Y. Zhang, J. Zhang, C. Pan, *J. Phys. Chem. C* 116 (2012) 7515–7519.
- [51] H. Tada, T. Mitsui, T. Kiyonaga, T. Akita, K. Tanaka, *Nat. Mater.* 5 (2006) 782.
- [52] L. Sun, Z. Zhao, Y. Zhou, L. Liu, *Nanoscale* 4 (2012) 613–620.
- [53] Y. Zhao, Y. Wei, X. Wu, H. Zheng, Z. Zhao, J. Liu, J. Li, *Appl. Catal. B* 226 (2018) 360–372.
- [54] X.S. Qu, H.W. Song, G.H. Pan, X. Bai, B. Dong, H.F. Zhao, Q.L. Dai, H. Zhang, R.F. Qin, S.Z. Lu, *J. Phys. Chem. C* 113 (2009) 5906–5911.
- [55] Y. Wei, J. Jiao, Z. Zhao, J. Liu, J. Li, G. Jiang, Y. Wang, A. Duan, *Appl. Catal. B* 179 (2015) 422–432.
- [56] W. Zhou, W. Li, J.Q. Wang, Y. Qu, Y. Yang, Y. Xie, K. Zhang, L. Wang, H. Fu, D. Zhao, *J. Am. Chem. Soc.* 136 (2014) 9280–9283.
- [57] H. Zhang, X. Quan, S. Chen, H. Yu, N. Ma, *Chem. Mater.* 21 (2009) 3090–3095.
- [58] W. Wang, T. An, G. Li, D. Xia, H. Zhao, J.C. Yu, P.K. Wong, *Appl. Catal. B* 217 (2017) 570–580.
- [59] W. Cui, J. Li, W. Cen, Y. Sun, S.C. Lee, F. Dong, *J. Catal.* 352 (2017) 351–360.
- [60] S.N. Haberreutinger, L. Schmidt-Mende, J.K. Stolarczyk, *Angew. Chem. Int. Ed.* 52 (2013) 7372–7408.
- [61] S. Liu, J. Yu, M. Jaroniec, *Chem. Mater.* 23 (2011) 4085–4093.
- [62] Z. Zheng, B. Huang, J. Lu, X. Qin, X. Zhang, Y. Dai, *Chem. Eur. J.* 17 (2011) 15032–15038.